



Title	Study on Novel Electrostatic Bi-directional Transducers to Realize Low Power MEMS Devices for Wireless Sensors
Author(s)	内藤, 康幸
Citation	大阪大学, 2019, 博士論文
Version Type	VoR
URL	<a href="https://doi.org/10.18910/73584">https://doi.org/10.18910/73584</a>
rights	
Note	

*The University of Osaka Institutional Knowledge Archive : OUKA*

<https://ir.library.osaka-u.ac.jp/>

The University of Osaka

Doctoral Dissertation

Study on Novel Electrostatic Bi-directional  
Transducers to Realize Low Power  
MEMS Devices for Wireless Sensors

Yasuyuki Naito

July 2019

Graduate School of Engineering

Osaka University







Doctoral Dissertation

Study on Novel Electrostatic Bi-directional  
Transducers to Realize Low Power  
MEMS Devices for Wireless Sensors

Yasuyuki Naito

July 2019

Graduate School of Engineering

Osaka University



## Table of Contents

### **Chapter 1. Introduction: Low Power MEMS Devices for Wireless Sensors**

1.1. Background of This Study	p. 1
1.2. Purpose of This Study	p. 5
1.3. Structure of This Thesis	p. 7
References	p. 12

### **Chapter 2. Low Voltage RF-MEMS Switching Devices using Vertical Comb-drive Actuation**

2.1. Introduction and Research Review	p. 17
2.2. Design	p. 18
2.2.1. Vertical Comb-drive Actuation	
2.2.2. Actuation Characteristics	
2.3. Fabrication	p. 26
2.3.1. Process Flow	
2.3.2. Structure Observation	
2.4. Measurement Result	p. 32
2.4.1. Capacitance and RF Characteristics	
2.4.2. Actuation Characteristics	
2.4.3. Continuous Drive Cycles Characteristics	
2.5. Discussion	p. 40
References	p. 42

## **Chapter 3. Laterally Movable Triple Electrodes Actuator toward Low Voltage RF-MEMS Switches**

3.1. Introduction and Research Review	p. 45
3.2. Design	p. 46
3.2.1. Effect of Laterally Movable Triple Electrodes Actuator	
3.2.2. Movable Electrode as RF Transmission Line	
3.2.3. Summary of Design	
3.3. Fabrication	p. 56
3.3.1. Process Flow	
3.3.2. Structure Observation	
3.4. Measurement Result	p. 61
3.5. Discussion	p. 64
References	p. 66

## **Chapter 4. High-Q Torsional Mode Si Triangular Beam Resonators Encapsulated using SiGe Thin Film**

4.1. Introduction and Research Review	p. 69
4.2. Design	p. 70
4.2.1. Torsional Mode Triangular Beam Resonator	
4.2.2. Wafer-level Thin Film Package	
4.3. Fabrication	p. 76
4.4. Measurement Result	p. 79
4.5. Discussion	p. 84
References	p. 86

**Chapter 5. Electrostatic MEMS Vibration Energy Harvesters inside of  
Tire Treads**

5.1. Introduction and Research Review	p. 89
5.2. Design	p. 91
5.2.1. Basic Concept of an Electrostatic MEMS Vibration Energy Harvester	
5.2.2. Electrode Configuration for High Power Generation	
5.2.3. Electret Structure for a High Charge Ratio on Output Electrodes	
5.3. Fabrication	p. 97
5.3.1. Process Flow	
5.3.2. Annealing Process for a Highly-Stable Inorganic Electret	
5.4. Measurement Result	p. 102
5.4.1. Sign-Wave Vibration	
5.4.2. Impact Vibration in Tire Tread	
5.5. Discussion	p. 109
References	p. 111

**Chapter 6. Conclusion** p. 115

**Acknowledgement** p. 119

**Publications Related to This Thesis** p. 120

**Other Publications** p. 122



## **Chapter 1. Introduction: Low Power MEMS Devices for Wireless Sensors**

### **1.1. Background of This Study**

It is expected to provide highly convenient functions and services by connecting all devices to a network. This is a concept called IoT (internet of things) and M2M (machine to machine) as shown in Figure 1.1 [1], and sensor network is a required technology to realize this. A huge number of sensors will be installed in the future, and so-called big data collected by the sensors will be used for various services. The concept of Trillion Sensors Universe is also presented [2]. There is a concern about the feasibility and cost of wiring to each sensor, therefore it is required to make the network and power supply wireless. Figure 1.2 shows configuration of autonomous wireless sensor module. A radio and a power generator in addition to the sensor are mounted on the sensor module. MEMS (micro-electro-mechanical systems) are expected technologies to realize higher performance of these devices.

MEMS technologies enable superior performance of RF (Radio frequency) front end. Tunable performance of RF-MEMS switching devices is useful to embody tunable filters, matching networks and phase shifters to adjust a RF circuit for the multi-band and multi-system wireless communication terminal, e.g. GSM (global system for mobile communications), IMT-2000 (international mobile telecommunication 2000) and wireless LAN (local area network) [3-5]. The switching devices are capacitors which are different from switches with RF performance such as

low insertion loss and high isolation [6].

RF-MEMS switches have a high potential to evolve terminals for wireless communication and wireless sensor networks. Superior performances in RF front-end involve low insertion loss, high isolation, and linear characteristics compared with conventional GaAs FET (field effect transistor) and PIN (P-intrinsic-N) diode switches. The low insertion loss contributes to high receiving sensitivity and low power consumption for mobile terminals.

Actuation forces used in the RF-MEMS switches are representatively electrostatic, piezoelectric, electromagnetic, and thermoelastic. The electrostatic actuator is the leading candidate because of its simple structure, CMOS (complementary metal-oxide-semiconductor) compatible process, and high generated force. In spite of these advantages, the RF-MEMS switches using the electrostatic actuator have disadvantages of relatively slow switching speeds over 10  $\mu$ s, high actuation voltages over 10 V, mechanical reliability, and larger footprint size than the semiconductor switches. They obstruct the RF-MEMS switches to be used in the wireless communication terminals. Low actuation voltage makes switching speed slow, on the other hand, a fast switching speed needs high actuation voltage [7-10].

Silicon-resonator based oscillators provide an attractive alternative to replace conventional frequency control devices and timing devices that are based on high quality factor ( $Q$ ) resonators such as quartz crystal, piezoelectric ceramic and SAW (surface acoustic wave) [11-14]. Quartz crystal resonators display high frequency stability but are difficult to be miniaturized and cannot offer an integrated solution. Silicon MEMS resonators on the other hand offer enhanced miniaturization, low

susceptibility to shock and vibration, and higher integration over conventionally used quartz crystal resonators. Drawbacks of MEMS-based oscillators remain the poor temperature stability, low phase noise and limited frequency accuracy. MEMS-based oscillators therefore appear suited to non-critical timing applications and applications where the signal-to-noise ratios are less important.

High- $Q$  MEMS resonators with low motional resistance and low driving voltage are advantageous to attain high frequency accuracy (and stability) of a reference oscillator with low power consumption (by the sustaining amplifier and the charge pump). A MEMS resonator operating in a wine-glass mode of vibration with a  $Q$ -factor of 161,000 and motional resistance of 11.73 k $\Omega$  has been reported, but it requires a rather high actuation voltage of 7 V [11]. Similar observations are made from the square-extensional mode resonator, which requires an actuation voltage of 100 V in order to obtain the low motional resistance of 4.47 k $\Omega$  [13].

In order to improve the driving safety of automobiles, the requirements of TPMS (tire pressure monitoring systems) have advanced worldwide, starting with the United States and Europe [15,16]. A tire sensor with the TPMS inside of tire tread enables gathering information of the road surface and tires for the detection of the degree of slippage. It is possible to control the attitude of the vehicle safely and comfortably. The tire sensor consists of not only a pressure sensor, but also an acceleration sensor and a temperature sensor, which improves the detection accuracy by analyzing the multifaceted data at a high frequency. It is necessary to supply stable power to the tire sensor during the life of tire because replacement of the power supply is not acceptable in consideration of user convenience and the reduction of cost.

An electrostatic vibration energy harvester is one of the expected candidates in power generation methods because the power output density of the piezoelectric type or electromagnetic type is relatively low, and the device size becomes large. The electrostatic type needs an external voltage source to apply potential on electrodes for electric field generation [17]. An electrical charge holding an electret can be used as an internal voltage source of an electrostatic type. The electret vibration energy harvesters are classified mainly as the in-plane overlapping type [18] and the out-of-plane gap-closing type [19]. Structural optimization is also reported, a smaller air gap between electrets and output electrodes [20], and a mechanical nonlinearity with a spring stopper [21,22]. In most of these works, vibration energy harvesters are evaluated under sinusoidal vibration, which rarely exists in the real environment from the application point of view. Stochastic noise-like vibration tests are reported in the experimental environment [23,24].

For the TPMS and the tire sensors, electret vibration energy harvesters have to be evaluated considering the real impact vibration inside of the tire tread. The previously reported output power was 4.5  $\mu\text{W}$  in the case of PSD (power spectral density) of impact vibration acceleration of  $7.3 \times 10^{-2} \text{ g}^2\cdot\text{Hz}^{-1}$  at a traveling speed of 50 km/h, and a mechanical resonance frequency of the harvester of 550 Hz [16]. An order of magnitude higher output is required to drive low power circuits.

## **1.2. Purpose of This Study**

Although realization of the autonomous wireless sensor module is expected, there are issues to reduce power consumption of the radio devices, the circuits devices and to increase power of the generator in order to compensate the whole power consumed in the module. This thesis aims to reveal solutions that realize low voltage RF-MEMS switches, low voltage MEMS resonators and high output MEMS energy harvesters for wireless sensors. Novel electrostatic bi-directional transducers are studied in order to reduce power consumption in the MEMS devices.

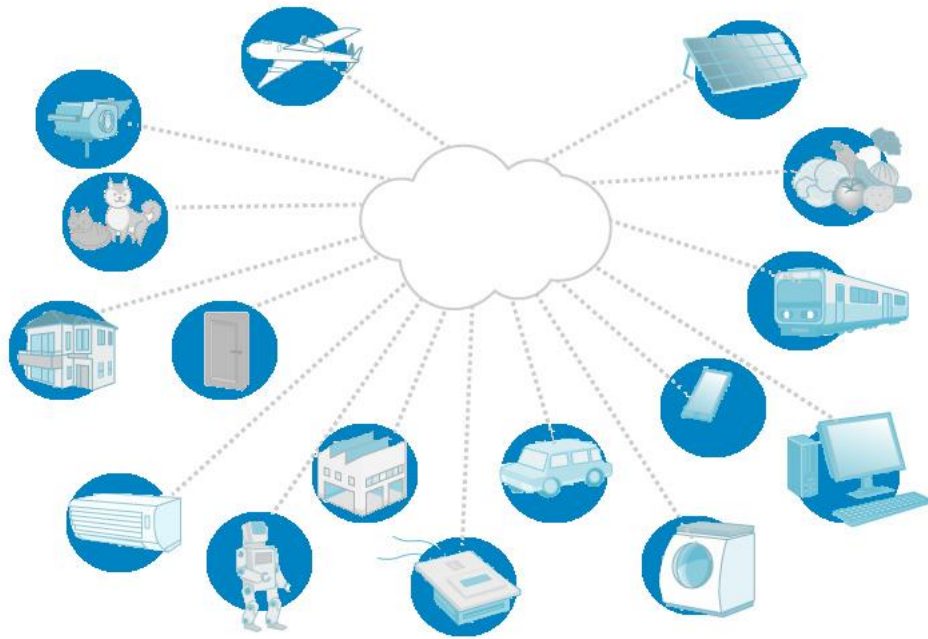


**Figure 1.1.** Conceptual diagram of IoT [1].

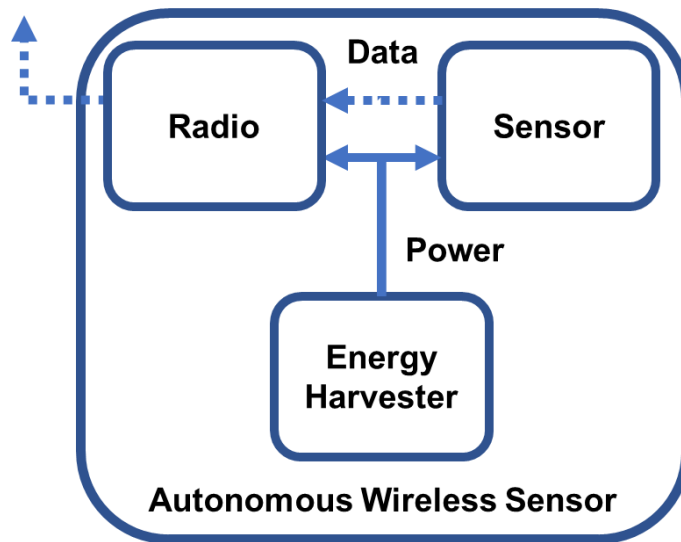


**Figure 1.2.** Configuration of autonomous wireless sensor module.

### 1.3. Structure of This Thesis

The relationship of each chapter showing on a photo of autonomous wireless sensor module is shown in Figure 1.3 [25]. The structure of this thesis is shown in Figure 1.4.

In Chapter 1, introduction and issues on low power MEMS devices for wireless sensors are described.

In Chapter 2, RF-MEMS switching device using vertical comb-drive actuation toward low voltage actuation is described. The switching devices, which comprise comb-drive electrodes, are actuated entirely by the electrostatic forces applied not only for the down-state but also for the up-state. The cost-effective MEMS process compatible with the CMOS process is demonstrated as well. The fabrication process is composed by adapting the CMOS 0.18  $\mu\text{m}$  BEOL (back end of line) process on 200 mm wafers. The MEMS process in the CMOS process enables the realization of passive devices integrated with active devices, which is effective for size and cost reduction. Two metal interconnection layers in the BEOL process are used for the MEMS process. Interconnection aluminum and inter-layer dielectric TEOS (tetraethoxysilane) are used as MEMS structural material and sacrificial material, respectively. The CMP (chemical mechanical polishing) process is implemented to planarize the sacrificial material surface. The structures are fabricated using a simple low-cost two-mask process. The characteristics of switching capacitors,  $C$ - $V$ , RF performance, switching speed and continuous drive cycles are measured on the fabricated devices. The capacitance ratio for the down-state / up-state is  $C_{\text{down}} / C_{\text{up}} = 5.4$ . The characteristics of switching speed response, actuation voltage in the down-

state and up-state are 4.5  $\mu\text{s}$ , 5 V and 8.0  $\mu\text{s}$ , 5 V, respectively. The switching speed is stable up to  $10^7$  cycles in spite of the fact that the unipolar voltage.

In Chapter 3, a novel actuator toward a low voltage actuation and fast response in RF-MEMS switches is described. The switch is comprised of laterally movable triple electrodes, which are bistable by electrostatic forces applied for not only the on-state, but also the off-state. The bistable triple electrodes enable the implementation of capacitive series and shunt type switches on a single switch, which leads to high isolation in spite of the small gap between the electrodes on the series switch. These features of the actuator are effective for a low voltage and fast response actuation in both the on- and off-state. The structure is designed in RF from a mechanical point of view. The laterally movable electrodes are achieved using a simple, low-cost two-mask process with 2.0  $\mu\text{m}$  thick sputtered aluminum. The characteristics of switching response time and actuation voltage are 5.0  $\mu\text{s}$  and 9 V, respectively.

In Chapter 4, an SOI-based (silicon on insulator) 20 MHz MEMS torsional resonator, wafer-level packaged using SiGe thin film and hermetically sealed using Al sputtering at 1Pa is described. The packaged resonators display a high quality factor (220,000) and a low motional resistance (12  $\text{k}\Omega$ ) for low driving voltage (1 V). The quality factor remains above 100,000 and the TCf (temperature coefficient of frequency) is measured to be  $-25 \text{ ppm}/^\circ\text{C}$  and linear over the temperature range of  $-40$  to  $+140$   $^\circ\text{C}$ . Successful operation of a CMOS-based oscillator using the MEMS torsional resonator as the frequency determining element is demonstrated.

In Chapter 5, an electret electrostatic MEMS vibration energy harvester for tire sensors mounted inside of the tire tread is described. The device is designed so as to linearly change an electrostatic capacitance

between the corrugated electret and output electrode according to the displacement of the proof mass. The electromechanical linearity is effective at reducing the power loss. The output power reaches  $495 \mu\text{W}$  under sinusoidal vibration despite the footprint size being as small as  $1 \text{ cm}^2$ . Under impact vibration inside of the tire tread, the output power reaches  $60 \mu\text{W}$  at a traveling speed of  $60 \text{ km/h}$ . It is revealed that a higher mechanical resonance frequency of the harvester adjusted within the frequency band of a low-power spectral density of impact vibration acceleration is effective for high efficiency harvest impact vibration energy.

In Chapter 6, solution on low power MEMS devices for wireless sensors is described. This thesis is concluded.

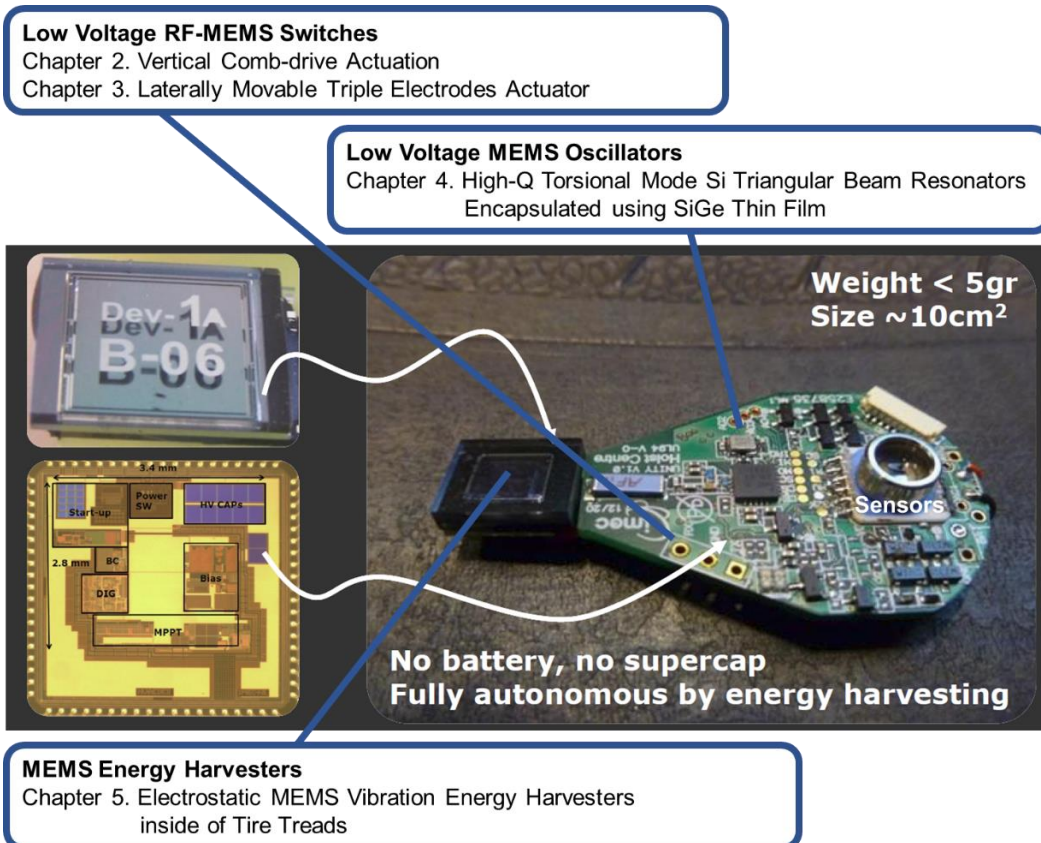


**Figure 1.3.** The relationship of each chapter showing on a photo of autonomous wireless sensor module [25].

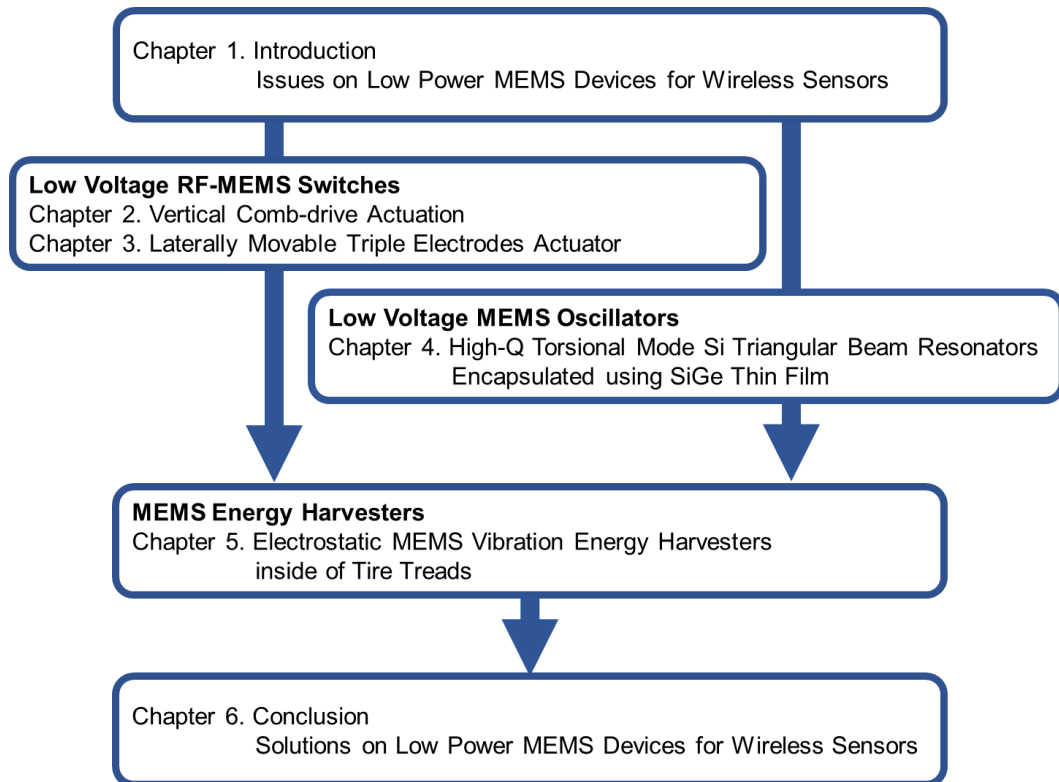


**Figure 1.4.** The structure of this thesis.

## References

1. Panasonic one-stop IoT/M2M solutions that utilize sensing and communication technology. Available online: <https://sol.panasonic.biz/cloud/iot-m2m/index.html> (in Japanese) (accessed on 10 May 2019).
2. Bryzek, J. Trillion Sensors: foundation for Abundance and internet of everything. Trillion Sensors Summit Japan, Tokyo, Japan, 20-21 February 2014.
3. Nguyen, C.T.-C.; Katehi, L.P.B.; Rebeiz, G.M. Micromachined devices for wireless communications. *Proc. IEEE* 1998, 86, 1756-1768.
4. Yao, J.J. RF MEMS from a device perspective. *J. Micromech. Microeng.* 2000, 10, R9-R38.
5. Tilmans, H.A.C.; De Raedt, W.; Beyne, E. MEMS for wireless communications: 'From RF-MEMS components to RF-MEMS-SiP'. *J. Micromech. Microeng.* 2003, 13, S139-S163.
6. Kuwabara, K.; Sato, N.; Shimamura, T.; Morimura, H.; Kodate, J.; Sakata, T.; Shigematsu, S.; Kudou, K.; Machida, K.; Nakanishi, M.; Ishii, H. RF CMOS-MEMS switch with low-voltage operation for single-chip RF LSIs. *Int. Electron Devices Meeting Tech. Dig.*, San Francisco, CA, USA, 11-13 December 2006; pp. 735-738.
7. Schlaak, H.F.; Arndt, F.; Hanke, M. Silicon-microrelay—a small signal relay with electrostatic actuator. *Proc. 45th Ann. Int. Relay Conf.*, Lake Buena, FL, USA, 1997; pp. 10.1-10.7.

8. Yao, Z.J.; Chen, S.; Eshelman, R.; Denniston, D.; Goldsmith, C.L. Micromachined low-loss microwave switches. *J. Microelectromech. Syst.* 1999, 8, 129-134.
9. Zavracky, P.M.; McGruer, N.E.; Morrison, R.H.; Potter, D. Microswitches and microrelays with a view toward microwave applications. *Int. J. RF Microw. Comput.-Aided-Eng.* 1999, 9, 338-347.
10. Pacheco, S.; Nguyen, C.T.; Katehi, L.P.B. Micromechanical electrostatic K-band switches. *IEEE MTT-S Int. Microwave Symp. Dig.*, Baltimore, MD, USA, 7-12 June 1998; vol. 3, pp. 1569-1572.
11. Nguyen, C.T.-C. MEMS technology for timing and frequency control. *IEEE Transactions on Ultrasonics, Ferroelectrics, and Frequency Control* 2007, 54, 251-270.
12. SiTime. Available online: <https://www.sitime.com> (accessed on 10 May 2019).
13. Kaajakari, V.; Mattila, T.; Oja, A.; Kiihamäki, J.; Seppä, H. Square-extensional mode single-crystal silicon micromechanical resonator for low-phase-noise oscillator applications. *IEEE Electron Device Letters* 2004, 25, 173-175.
14. van Beek, J.T.M.; Puers, R. A review of MEMS oscillators for frequency reference and timing applications. *J. Micromech. Microeng.* 2012, 22, 013001.
15. Löhndorf, M.; Kvisterøy, M T.; Westby, E.; Halvorsen, E. Evaluation of energy harvesting concepts for tire pressure monitoring systems. In *Proceedings of the PowerMEMS 2007, Freiburg, Germany, 28-29 November 2007*; pp. 331-334.

16. Westby, E.R.; Halvorsen, E. Design and modeling of a patterned-electret-based energy harvester for tire pressure monitoring systems. *IEEE/ASME Trans. Mechatron.* 2012, 17, 995-1005.
17. Jones, T.B. Lumped parameter electromechanics of electret transducers. *IEEE Trans. Acoust. Speech Signal Process.* 1974, 22, 141-145.
18. Suzuki, Y. Recent progress in MEMS electret generator for energy harvesting. *IEEJ Trans. Electr. Electron. Eng.* 2011, 6, 101-111.
19. Boisseau, S.; Despesse, G.; Seddik, B.A. Electrostatic conversion for vibration energy harvesting. In *Small-Scale Energy Harvesting*; Lallart, M., Ed.; IntechOpen: London, UK, 2012; pp. 91–134, ISBN 978-953-51-0826-9.
20. Asanuma, H.; Hara, M.; Oguchi, H.; Kuwano, H. Air gap optimization for output power and band width in out-of-plane vibration energy harvesters employing electrets. *J. Micromech. Microeng.* 2015, 25, 104013.
21. Tao, K.; Lye, S.W.; Miao, J.; Tang, L.; Hu, X. Out-of-plane electret-based MEMS energy harvester with the combined nonlinear effect from electrostatic force and a mechanical elastic stopper. *J. Micromech. Microeng.* 2015, 25, 104014.
22. Asanuma, H.; Hara, M.; Oguchi, H.; Kuwano, H. Nonlinear restoring force of spring with stopper for ferroelectric dipole electret-based electrostatic vibration energy harvesters. *AIP Adv.* 2016, 6, 075206.
23. Basset, P.; Galayko, D.; Cottone, F.; Guillemet, R.; Blokhina, E.; Marty, F.; Bourouina, T. Electrostatic vibration energy harvester with combined effect of electrical nonlinearities and mechanical impact. *J. Micromech. Microeng.* 2014, 24, 035001.

24. Zhang, Y.; Luo, A.; Xu, Y., Wang, T.; Zhang, A.; Wang, F. Electret-based electrostatic energy harvesting device with the MEMS technology. In Proceedings of the 2016 12th IEEE/ASME International Conference on Mechatronic and Embedded Systems and Applications (MESA), Auckland, New Zealand, 29-31 August 2016; pp. 1-6.
25. van Schaijk, R.; Elfrink, R.; Oudenhoven, J.; Pop, V.; Wang, Z.; Renaud, M. A MEMS vibration energy harvester for automotive applications. In Proceeding of the SPIE Microtechnologies, Grenoble, France, 24-26 April 2013.



## **Chapter 2. Low Voltage RF-MEMS Switching Devices using Vertical Comb-drive Actuation**

### **2.1. Introduction and Research Review**

MEMS technologies enable superior performance of RF front end. Tunable performance of RF-MEMS switching devices is useful to embody tunable filters, matching networks and phase shifters to adjust a RF circuit for the multi-band and multi-system wireless communication terminal, e.g. GSM, IMT-2000 and wireless LAN [1-3]. The switching devices demonstrated in this thesis are capacitors which are different from switches with RF performance such as low insertion loss and high isolation [4].

Electromechanical forces used to drive the MEMS actuators are electrostatic, thermoelastic, piezoelectric and electromagnetic. The actuators using the electrostatic force are the leading candidates because of simple structure and material. Despite these advantages, the devices suffer from relatively slow switching speeds and high actuation voltages ultimately making them unsuitable for use in wireless communication terminals [5-8]. It was verified that a low-cost vertical comb-drive actuation is effective for low voltage actuation, fast response in MEMS devices [9].

The CMOS compatible MEMS process is important for reducing the fabrication cost using the semiconductor mass-production line and small multi-function devices integrating MEMS with CMOS devices. Photoresist is used as a sacrificial material to make movable parts because the sacrificial material can be removed using dry etching of oxygen plasma ashing to avoid stiction due to a wet process [10]. In the case of using sputtered

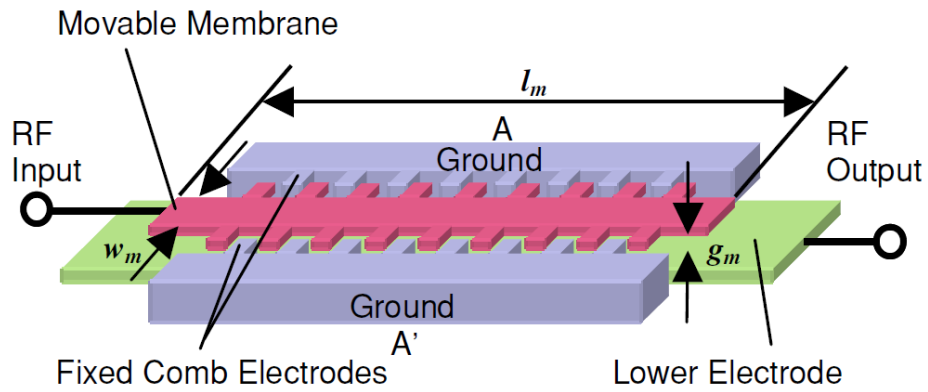
material as a MEMS structural layer, such as aluminum, it is undesirable to deposit the material over the photoresist because of contamination issues. According to the process condition of temperature and plasma power, out-gas from the photoresist is responsible for the contamination issues in the deposition chamber leading to quality degradation of the deposited film.

The fabrication process has to be designed using a suitable material in the CMOS line so that the MEMS process does not make a big change to the conventional semiconductor process. The fabrication method of RF-MEMS switching devices in the BEOL process using sacrificial silicon oxide is demonstrated. The effect of vertical comb-drive actuation is also described including the measurement results of the fabricated devices.

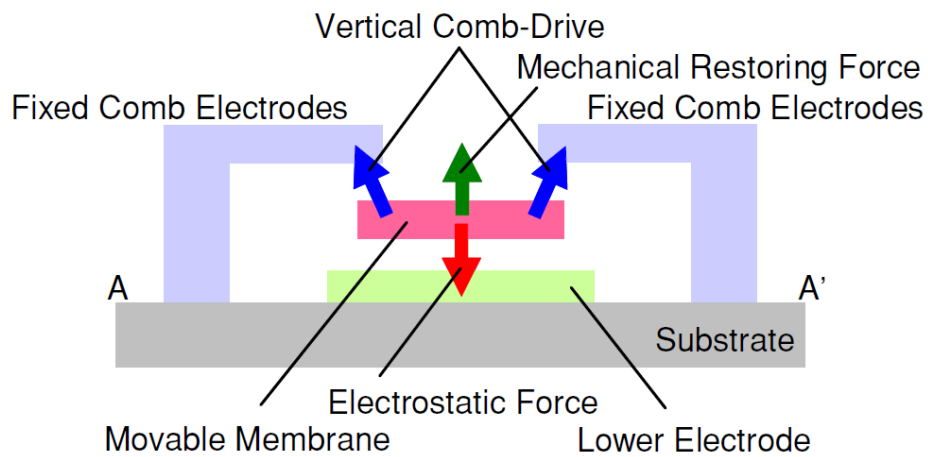
## **2.2. Design**

### **2.2.1. Vertical Comb-drive Actuation**

The schematic diagram of a switching device as described in this chapter is shown in Figure 2.1. The switching devices were designed as a capacitive series configuration. The comb-drive electrodes and the lower electrodes allow the suspended membrane to move vertically upward as well as downward entirely by electrostatic forces, thus enabling a fast overall response in MEMS devices.



(a)



(b)

**Figure 2.1.** Schematic diagram of the RF-MEMS switching device using vertical comb-drive actuation: (a) overview; (b) cross-sectional view along A–A' in (a).

### 2.2.2. Actuation Characteristics

The actuation characteristics are calculated with the dynamic analysis equation described as [11]:

$$m \frac{d^2 z}{dt^2} + b \left( 1.2 - \frac{z}{g_m} \right)^{-\frac{3}{2}} \frac{dz}{dt} + kz = F_{\text{down}} - F_{\text{up}} \quad (2.1)$$

where  $m$  is the mass of the movable membrane,  $z$  is the displacement from the up-state position,  $b$  is the damping coefficient, which is dominated by the squeeze-film damping under the membrane,  $g_m$  is the gap between the movable membrane and the lower electrode, and  $k$  is the spring constant of the movable membrane.  $F_{\text{down}}$  is the electrostatic force applied between the movable electrode and the lower electrode into the down-state,  $F_{\text{up}}$  is the electrostatic force applied between the comb electrodes of the movable membrane and the fixed comb electrodes into the up-state. In the down-state,  $F_{\text{up}}$  is zero.

The  $F_{\text{up}}$  depends on capacitance change of the comb electrodes, which is expressed by:

$$F_{\text{up}} = \frac{1}{2} \frac{\partial C_c}{\partial z} V_{\text{up}}^2 \quad (2.2)$$

where  $C_c$  is the capacitance of the comb electrodes,  $V_{\text{up}}$  is the applied voltage to the comb electrodes. The simulated capacitance of one pair comb electrode is shown in Figure 2.2. The capacitance is calculated with FEM (finite element method, CoventorWare). The comb electrodes are designed to overlap in the down-state to generate the capacitance change and the electrostatic force.

The spring constant of the movable membrane affects pull-in

voltage and switching speed. According to an expression for fixed-fixed beam, the spring constant  $k$  depends on physical dimensions, residual stress, and intrinsic material stiffness, given by the following [12]:

$$k = 32Ew_m \left(\frac{t_m}{l_m}\right)^3 + 8\sigma(1 - \nu)w_m \left(\frac{t_m}{l_m}\right) \quad (2.3)$$

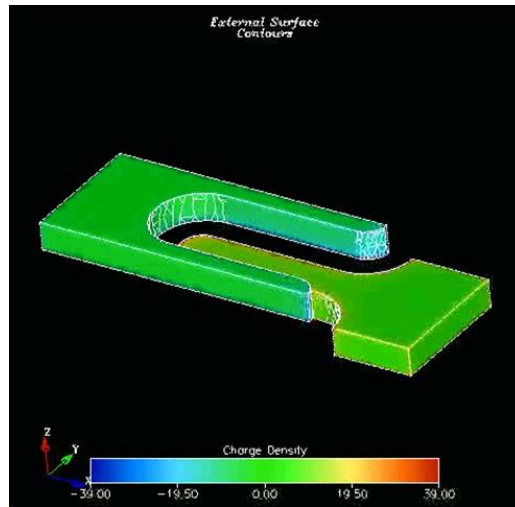
where  $w_m$ ,  $t_m$ , and  $l_m$  are width, thickness, and length, respectively;  $E$  is the Young's modulus;  $\nu$  is the Poisson's ratio; and  $\sigma$  is the residual stress of the movable membrane. The length is effective in order to reduce the spring constant because the spring constant depends inversely on the length by the factor of 3 in the case of low residual stress.

The simulated down response time and insertion loss as a function of length of the movable electrode are shown in Figure 2.3. An electromagnetic field analysis (Agilent Momentum) is used for the insertion loss simulation. The calculation parameters are  $w_m = 5 \mu\text{m}$ ,  $t_m = 0.8 \mu\text{m}$ ,  $g_m = 0.6 \mu\text{m}$ , and the dielectric material inserted between two signal lines is  $\text{Al}_2\text{O}_3$  (thickness  $t_d = 10 \text{ nm}$ , dielectric constant  $\epsilon_r = 10$ ). The insertion loss of the series switch depends on capacitance determined by lateral overlap area between the movable membrane and the lower electrode. If the length becomes longer, the insertion loss decreases as a result of the increase of the capacitance. The response time becomes shorter as a result of the decrease of the spring constant, according to Equation (2.3). Beyond a certain length, as the membrane gets longer, the insertion loss increases again as a result of the increased resistance of the electrodes. In this situation, the capacitive coupling loss is not more than the resistive loss.

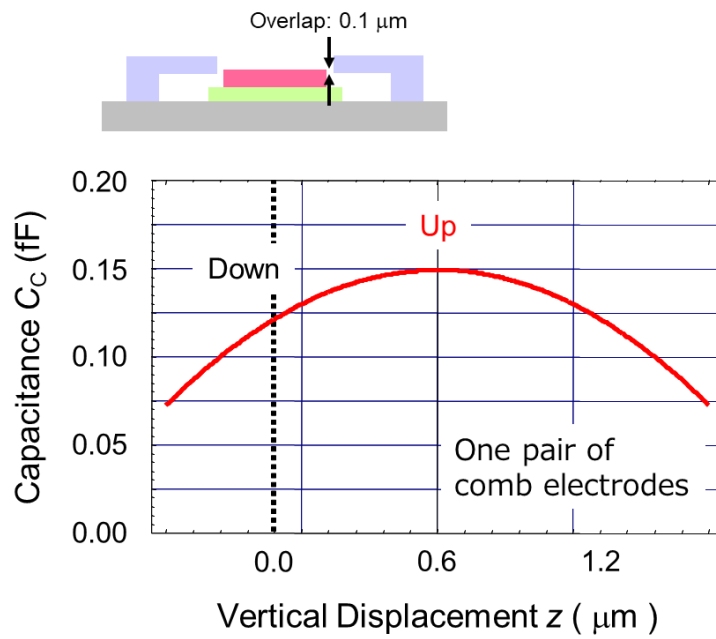
The specifications of the response time and the actuation voltage are set several microseconds and several volts less than those of the switching time of the RF circuit and the power source voltage to the

switching devices, 5.0  $\mu\text{s}$  and 5.0 V in terms of the pull-down response. The length is optimized:  $l_m = 600 \mu\text{m}$  to achieve the pull-down response time 4.8  $\mu\text{s}$  at a 5 V actuation voltage. The designed specifications are summarized in Table 2.1.

The residual stress was determined by the mechanical resonant frequency of the fabricated movable membrane measured by a laser Doppler interferometer. The measured flexural mode resonance is shown in Figure 2.4. The flexural mode resonant frequency of the first, second and third are 116 kHz, 233 kHz and 353 kHz, respectively. The first flexural mode resonant frequency as a function of the residual stress is calculated with FEM simulation to estimate the residual stress, the result of which is shown in Figure 2.5. The residual stress is about  $\sigma = 50 \text{ MPa}$  tensile stress at the measured resonant frequency. In this case, the spring constant is estimated to be  $k = 2.0 \text{ N m}^{-1}$ .



(a)



(b)

**Figure 2.2.** Simulated capacitance of one pair comb electrode: (a) FEM model; (b) capacitance as a function of vertical displacement of movable membrane.

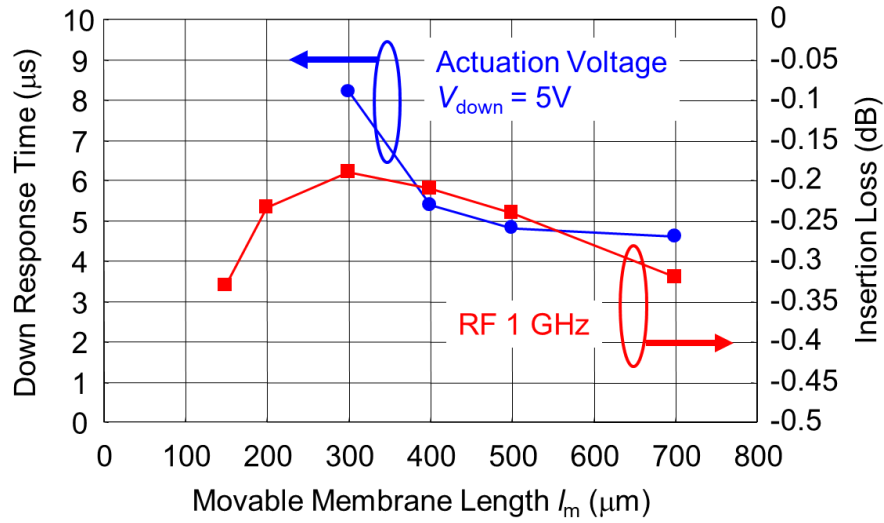


**Figure 2.3.** Simulated down response time and insertion loss as a function of length of movable membrane.

**Table 2.1.** Designed specifications of vertical comb-drive actuator in RF-MEMS switching devices.

<b>Movable Membrane</b>	
Length ( $l_m$ )	600 $\mu\text{m}$
Width ( $w_m$ )	5.0 $\mu\text{m}$
Thickness ( $t_m$ )	0.8 $\mu\text{m}$
Gap ( $g_m$ )	0.6 $\mu\text{m}$
<b>Comb Electrodes</b>	
Length ( $l_c$ )	5.0 $\mu\text{m}$
Width ( $w_c$ )	1.0 $\mu\text{m}$
Thickness ( $t_c$ )	0.8 $\mu\text{m}$
Gap ( $g_c$ )	0.6 $\mu\text{m}$

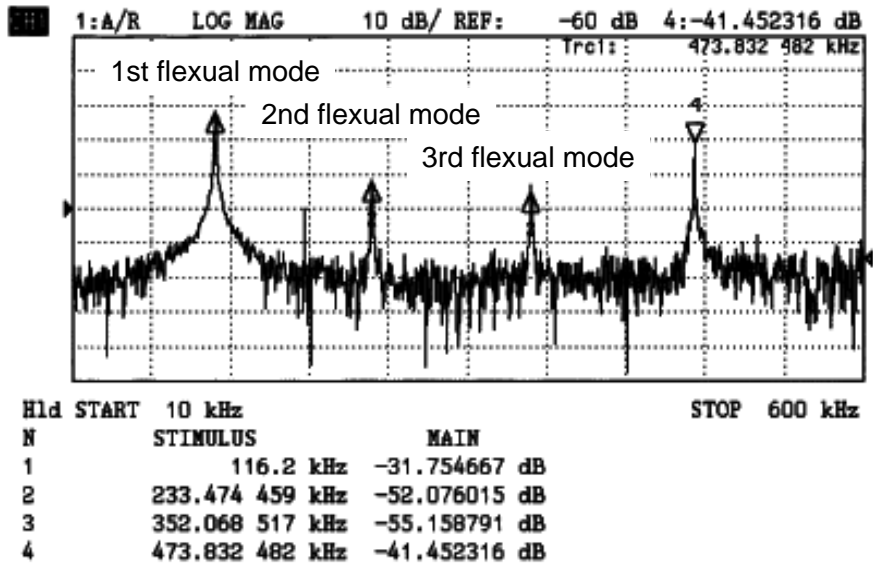


**Figure 2.4.** Flexural mode mechanical resonant frequency results of the fabricated movable membrane.

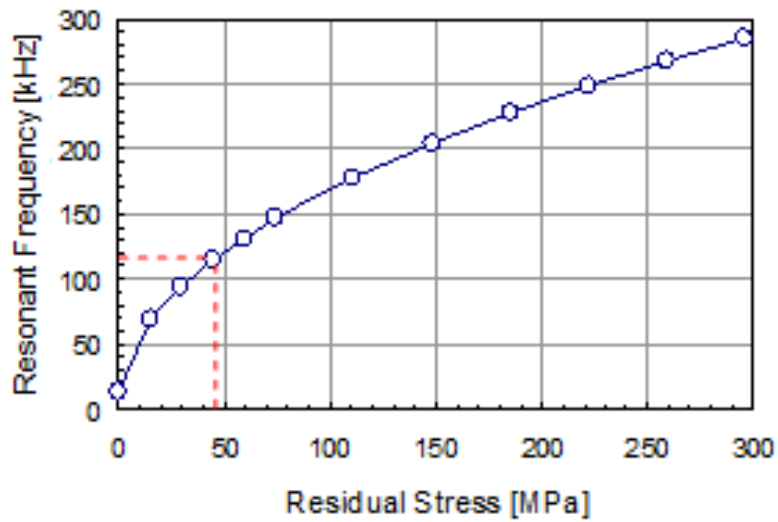


**Figure 2.5.** Simulated mechanical resonant frequency of the first flexural mode as a function of residual stress of the movable membrane.

## 2.3. Fabrication

### 2.3.1. Process Flow

The fabrication process flow for MEMS devices in the CMOS line is shown in Figure 2.6. The structures were fabricated using a simple low-cost two-mask process in a 0.18  $\mu\text{m}$  CMOS BEOL line. The switching devices were fabricated on a 200 mm diameter silicon substrate with the isolation oxide layer. The lower electrodes were fabricated by sputtering 0.8  $\mu\text{m}$  aluminum alloy (Al-0.5%Cu) and etched using RIE (reactive ion etching). TEOS was deposited as a sacrificial material using PECVD (plasma-enhanced chemical vapor deposition) and the surface is flattened using CMP to remove a step of the lower electrode.

The process condition of the CMP process was optimized to determine the gap between the lower electrode and the movable electrode, which is the critical dimension affecting the characteristics of the switching devices. A high accuracy of flatness, uniformity and surface roughness is required; therefore, the pattern of the lower electrode was designed as small as possible to avoid a global step from the CMP process. Controllability of the polishing thickness was tuned for the designed gap of 0.6  $\mu\text{m}$  on top of the lower electrode. The CMP uniformity relating to the yield over 80 % on a 200 mm diameter substrate was  $0.60 \pm 0.06 \mu\text{m}$  (9.8 %) which means distribution of the pull-down response time  $4.8 \pm 1.6 \mu\text{s}$  (32.4 %) because the pull-down response time is directly proportional to the gap to the power of 3 [12].

The movable electrode and the fixed comb electrodes were

fabricated by sputtering 0.8  $\mu\text{m}$  aluminum alloy (Al-0.5%Cu). The low residual stress about  $\sigma = 50$  MPa tensile stress was achieved with low temperature Al sputtering below 200  $^{\circ}\text{C}$  to avoid thermal stress. The 0.6  $\mu\text{m}$  air gaps of the comb electrodes were patterned with photolithography using i-line stepper and RIE. Release holes of 1  $\mu\text{m}$  in diameter were formed on the fixed comb electrodes and the supports of the membrane beam to facilitate the release of the membrane.

Finally, the sacrificial material was removed using vapor HF (hydrofluoric) acid to eliminate the stiction of the movable electrode and the etching process was stopped to leave the TEOS at the support area underneath the fixed electrodes.  $\text{CH}_3\text{OH}$  was introduced to decrease attack on the surface of the aluminum and post-anneal after the release step was processed to remove the fluoride residue from the device surface. The aluminum electrodes are covered with the  $\text{Al}_2\text{O}_3$  native oxide dielectric layer.

### 2.3.2. Structure Observation

The cross-sectional view of the structure before the release process is shown in Figure 2.7. The process flow following Figure 2.6 can be checked and the successfully finished CMP process can be observed. The thickness of the sacrificial TEOS on top of the lower electrode is consistent with the designed value of 0.6  $\mu\text{m}$ .

The SEM (scanning electron microscope) images of the fabricated switching devices are shown in Figure 2.8. It is confirmed that the sacrificial layer is removed, and the air bridge structure is fabricated. The movable electrode goes down to the lower electrode because of the breakdown in the

middle of the movable electrode for observation. The fixed comb electrodes structure stands up stably.

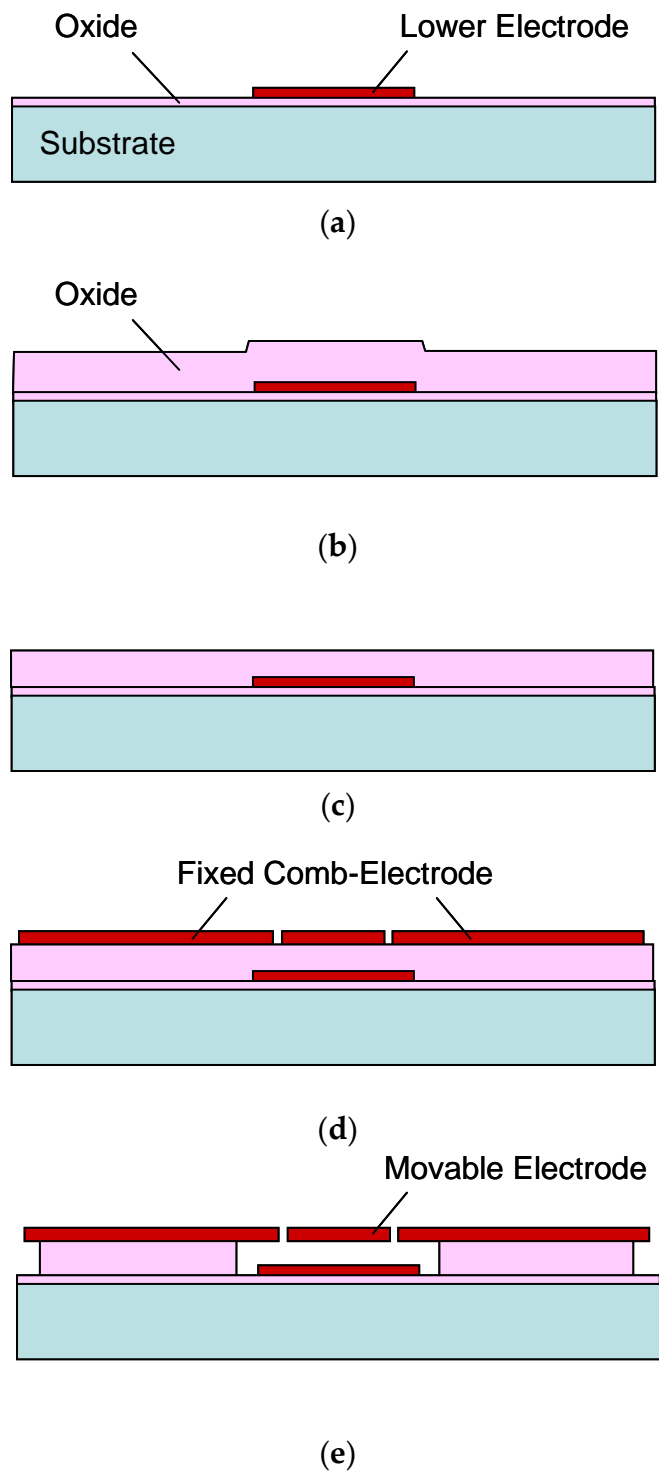


**Figure 2.6.** MEMS fabrication process flow in the CMOS line: (a) formation of isolation oxide and Al electrodes; (b) TEOS deposition; (c) CMP planarization; (d) Al electrodes; (e) release as actuator.

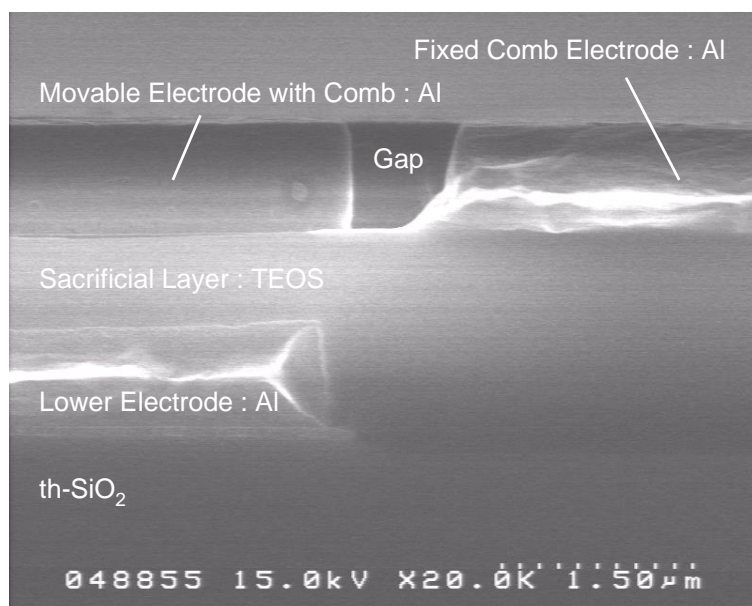
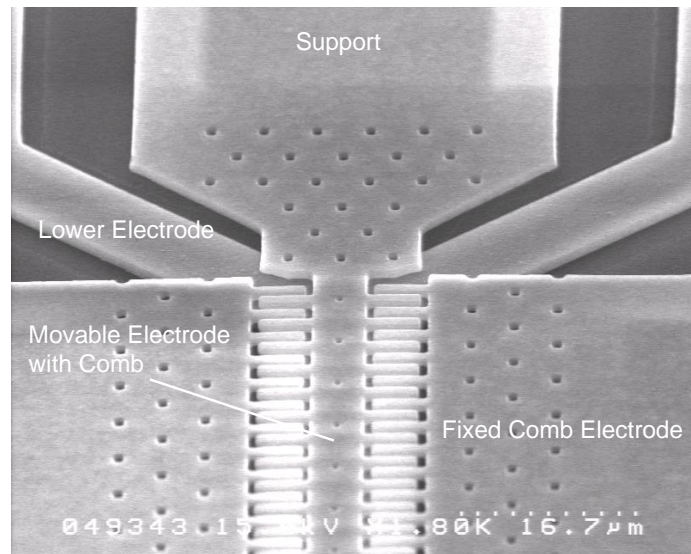
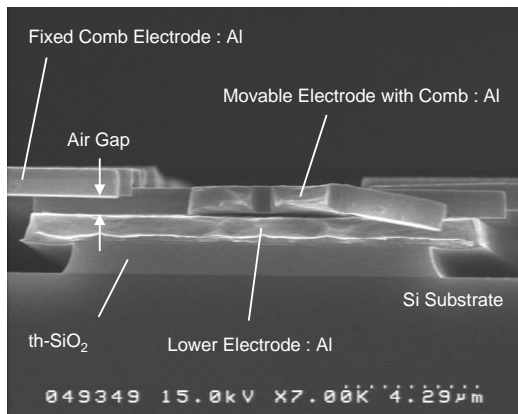


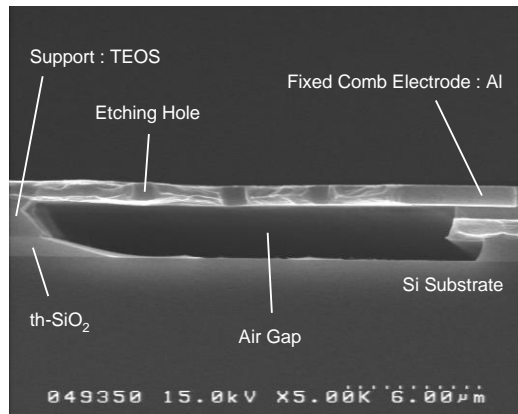
**Figure 2.7.** SEM images of cross-sectional view before the release process.



(a)



(b)



(c)

**Figure 2.8.** SEM images of fabricated switching devices: (a) close-up of the support area; (b) cross-sectional view of the movable electrode; (c) cross-sectional view of the fixed comb electrode along A-A' in Figure 2.1a.

## 2.4. Measurement Result

### 2.4.1. Capacitance and RF Characteristics

The measured capacitance as a function of the control voltage is shown in Figure 2.9. The capacitance of the up-state is  $C_{up} = 0.095$  pF. Increasing the control voltage, the capacitance between the lower electrode and the movable electrode increases after pull-in and the capacitance of the down-state  $C_{down} = 0.514$  pF is saturated at 10 V. The capacitance ratio at the down-state / up-state is  $C_{down} / C_{up} = 5.4$ . The measured pull-in voltage is  $V_p = 2.7$  V, which is consistent with the simulated pull-in voltage 2.3 V. The measured pull-off voltage is 1.8 V decreasing the control voltage.

The measured transmission parameter  $S_{21}$  as a function of frequency is shown in Figure 2.10.  $S_{21}$  in the down-state and the up-state is  $-2.4$  dB and  $-15.1$  dB at 5 GHz, respectively.

### 2.4.2. Actuation Characteristics

The response time of the fabricated switching devices was measured. The measurement setup and applied control signals are shown in Figure 2.11 and Table 2.2. The turn-down and turn-up switching waveforms for the fabricated switching devices are shown in Figures 2.12 and 13. The control voltage is applied with a 1 kHz rectangular waveform.

The measured response time into the down-state is  $4.5$   $\mu$ s at a 5 V actuation voltage, and it is  $11.2$   $\mu$ s for the up-state with no DC voltage applied and actuated only by the mechanical restoring force of the movable

electrode. However, when the same device was actuated using the vertical comb-drive electrodes, the response time reduced to 8.0  $\mu\text{s}$  at a 5 V actuation voltage, with a total improvement of 3.2  $\mu\text{s}$  into the up-state.

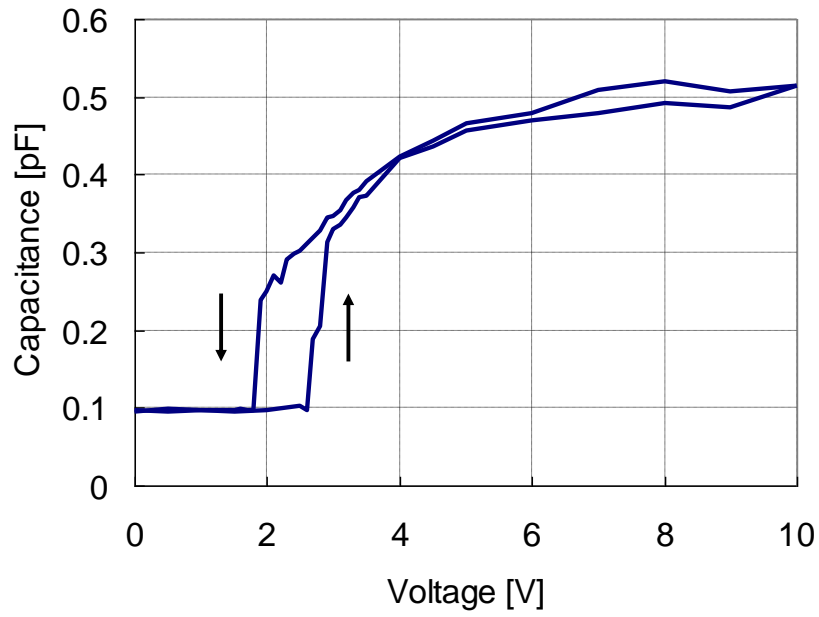


**Figure 2.9.** C-V measurement results of fabricated switching devices.

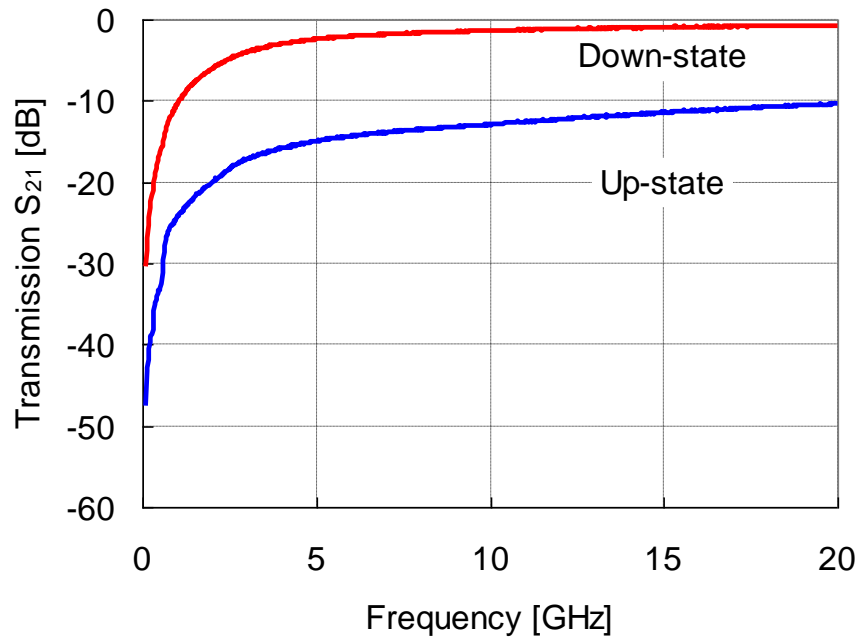


**Figure 2.10.** RF characteristics measurement results of fabricated switching devices.

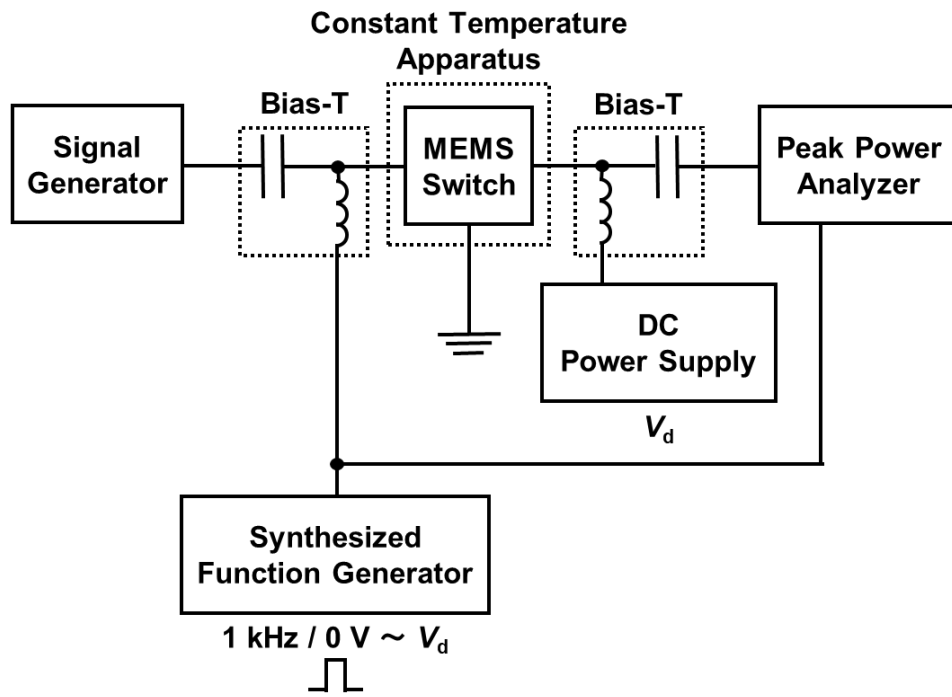


**Figure 2.11.** Switching speed measurement setup.

**Table 2.2.** Applied control signals of vertical comb-drive actuator.

	Lower Electrode	Movable Membrane	Fixed Comb Electrodes
Down	High	Low	Low
Up	High	High	Low

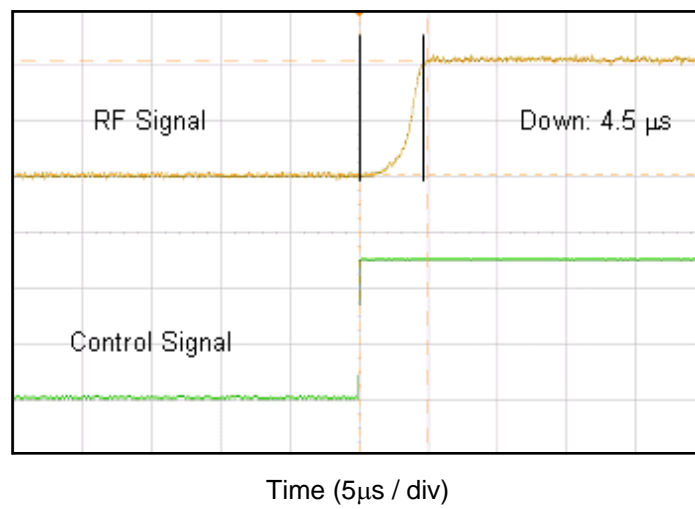
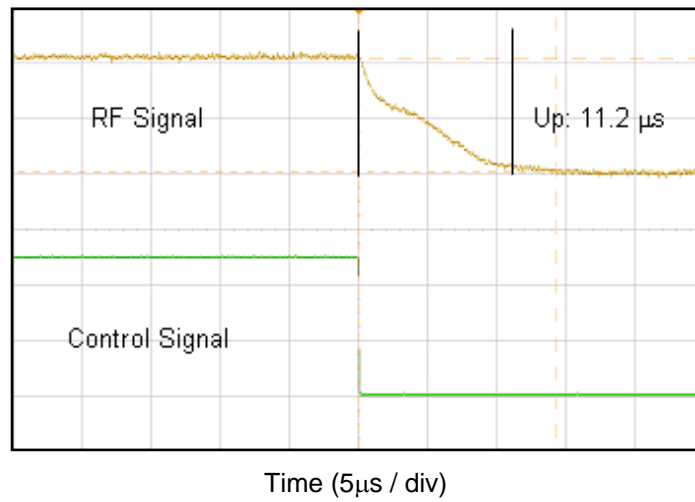
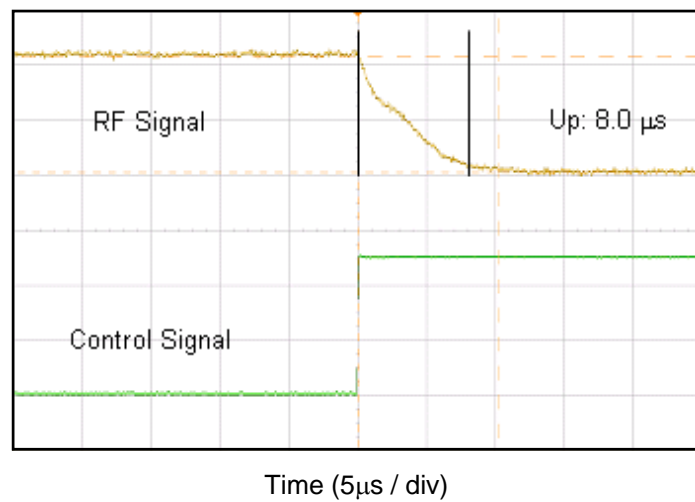


**Figure 2.12.** Switching speed measurement results of fabricated switching devices: turn-down at 5 V.



(a)



(b)

**Figure 2.13.** Switching speed measurement results of fabricated switching devices: (a) turn-up without vertical comb-drive actuation; (b) turn-up at 5 V with vertical comb-drive actuation.

### 2.4.3. Continuous Drive Cycles Characteristics

The continuous drive cycles measurement was performed at room temperature, humidity 20 % in the constant temperature and humidity apparatus. The control voltage is applied with 5 V unipolar actuation, 1 kHz rectangular waveform and 50 % duty cycle.

The turn-down and turn-up response time as a function of the continuous drive cycles is shown in Figure 2.14. The measured response time into the down-state was stable around 4.5  $\mu\text{s}$  up to  $10^9$  cycles. The response time into the up-state pulled up by the comb-drive actuation was stable around 8.0  $\mu\text{s}$  up to  $10^7$  cycles. The response time into the up-state degraded and become longer to 15.0  $\mu\text{s}$  from an order of  $10^8$  cycles and 37  $\mu\text{s}$  at  $10^9$  cycles.

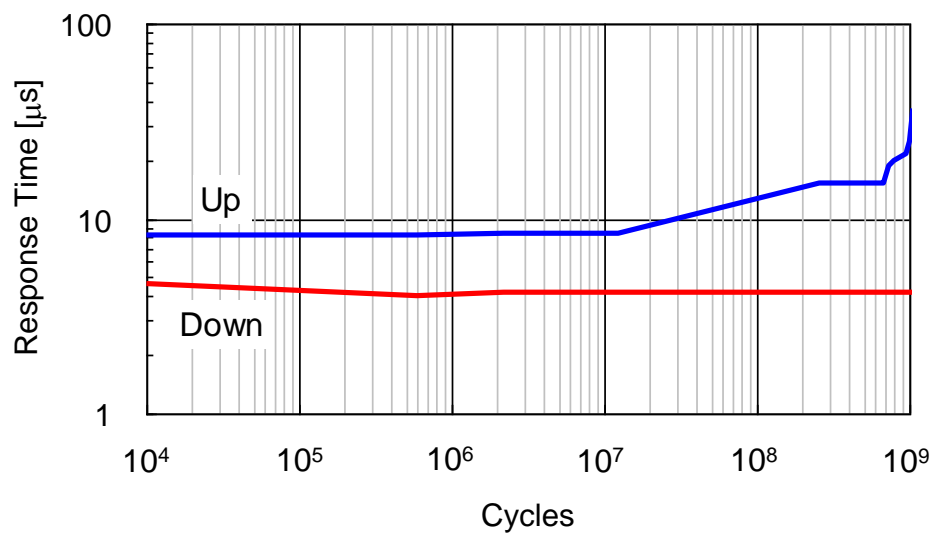


**Figure 2.14.** Continuous drive cycles measurement results of fabricated switching devices.

## 2.5. Discussion

In this chapter, the capacitive RF-MEMS switching devices utilizing comb-drive electrodes for low voltage actuation and fast response were described. The process flow for MEMS fabrication was optimized considering compatibility in the 0.18  $\mu\text{m}$  CMOS BEOL process on a 200 mm substrate toward low-cost fabrication and integrated MEMS devices with CMOS circuits. Aluminum of interconnect material is used as a MEMS structural material, and TEOS for isolation between interconnects is used as sacrificial material for MEMS fabrication. CMP is introduced to the MEMS process for planarization of the sacrificial layer surface to adjust the gap between the lower electrode and the movable electrode, which affects the actuation voltage and the switching speed. Vapor HF is used to remove the sacrificial silicon oxide layer to avoid stiction due to a wet process.

The switching devices were fabricated using a simple low-cost two-mask process. The comb-drive electrodes and the lower electrodes allow the suspended membrane to move vertically upward as well as downward entirely by the electrostatic forces, thus enabling a fast overall response in MEMS devices.

The measured C-V and RF characteristics were  $C_{\text{down}} / C_{\text{up}} = 0.514 \text{ pF} / 0.095 \text{ pF} = 5.4$ , and the transmission parameter  $S_{21}$  in the down-state and the up-state is  $-2.4 \text{ dB}$  and  $-15.1 \text{ dB}$  at 5 GHz, respectively. The measured responses were 4.5  $\mu\text{s}$  into the down-state and 8.0  $\mu\text{s}$  into the up-state with 5 V actuation voltage. The continuous drive cycles characteristics were measured up to  $10^9$  cycles, in which stable actuation was observed up to  $10^7$ ; degradation of actuation into the up-state was observed from an order of

$10^8$  cycles. The possible cause for the degradation is stiction due to dielectric charging at a contact interface by the unipolar voltage actuation.

One of the issues for commercialization is packaging technology for high reliability. A hermetic package is required in order to avoid aluminum oxidation and adhesion of the movable electrode due to humidity (so-called stiction). In the case of vacuum, a chattering phenomenon occurs in which the movement of the movable electrode cannot be settled down because there is no air viscosity. For this reason, it is preferable to replace with an inert gas such as nitrogen. The MEMS packaging technology is also developed with chip-level and wafer-level bonding technology.

It was revealed that the MEMS devices using the effective comb-drive actuation for low voltage actuation and fast response are embodied with the CMOS process, which could contribute to low-cost integrated RF-MEMS switches, switched capacitors and MEMS devices in circuits for expected applications.

## References

1. Nguyen, C.T.-C.; Katehi, L.P.B; Rebeiz, G.M. Micromachined devices for wireless communications. Proc. IEEE 1998, 86, 1756-1768.
2. Yao, J.J. RF MEMS from a device perspective. J. Micromech. Microeng. 2000, 10, R9-R38.
3. Tilmans, H.A.C.; De Raedt, W.; Beyne, E. MEMS for wireless communications: 'from RF-MEMS components to RF-MEMS-SiP'. J. Micromech. Microeng. 2003, 13, S139-S163.
4. Kuwabara, K.; Sato, N.; Shimamura, T.; Morimura, H.; Kodate, J.; Sakata, T.; Shigematsu, S.; Kudou, K.; Machida, K.; Nakanishi, M.; Ishii, H. RF CMOS-MEMS switch with low-voltage operation for single-chip RF LSIs. Int. Electron Devices Meeting Tech. Dig., San Francisco, CA, USA, 11-13 December 2006; pp. 735-738.
5. Schlaak, H.F.; Arndt, F.; Hanke, M. Silicon-microrelay—a small signal relay with electrostatic actuator. Proc. 45th Ann. Int. Relay Conf., Lake Buena, FL, USA, 1997; pp. 10.1-10.7.
6. Yao, Z.J.; Chen, S.; Eshelman, R.; Denniston, D.; Goldsmith, C.L. Micromachined low-loss microwave switches. J. Microelectromech. Syst. 1999, 8, 129-134.
7. Zavracky, P.M.; McGruer, N.E.; Morrison, R.H.; Potter, D. Microswitches and microrelays with a view toward microwave applications. Int. J. RF Microw. Comput.-Aided-Eng. 1999, 9, 338-347.
8. Pacheco, S.; Nguyen, C.T.; Katehi, L.P.B. Micromechanical electrostatic K-band switches. IEEE MTT-S Int. Microwave Symp. Dig., Baltimore, MD, USA, 7-12 June 1998; vol. 3, pp. 1569-1572.

9. Naito, Y.; Shimizu, N.; Hashimura, A.; Nakamura, K.; Nakanishi, Y. A low-cost vertical comb-drive approach to low voltage and fast response RF-MEMS switches. Proc. 34th European Microwave Conf., Amsterdam, The Netherlands, 12-14 October 2004; vol. 3, pp. 1149-1152.
10. Tilmans, H.A.C.; Ziad, H.; Jansen, H.; Di Monaco, O.; Jourdain, A.; De Raedt, W.; Rottenberg, X.; De Backer, E.; Decaussemaeker, A.; Baert, K. Wafer-level packaged RF-MEMS switches fabricated in a CMOS fab. Int. Electron Devices Meeting Tech. Dig., Washington, DC, USA, 2-5 December 2001; pp. 921-924.
11. Muldavin, J.B.; Rebeiz, G.M. Nonlinear electromechanical modeling of MEMS switches. IEEE MTT-S Int. Microwave Symp. Dig., Phoenix, AZ, USA, 20-24 May 2001; pp. 2119-2122.
12. Rebeiz, G.M. Mechanical modeling of MEMS devices: Static analysis. In RF MEMS Theory, Design, and Technology; Wiley & Sons, Inc.: Hoboken, NJ, USA, 2003; Chapter 2, Section 2.1, p. 27, 9780471201694.



## **Chapter 3. Laterally Movable Triple Electrodes Actuator toward Low Voltage RF-MEMS Switches**

### **3.1 Introduction and Research Review**

RF-MEMS switches have a high potential to evolve terminals for wireless communication and wireless sensor networks. Superior performances in RF front-end involve low insertion loss, high isolation, and linear characteristics compared with conventional GaAs FET and PIN diode switches. The low insertion loss contributes to high receiving sensitivity and low power consumption for mobile terminals. MEMS switched capacitors are also applied to reconfigurable circuits that enable mobile terminals to adapt to multi-band systems [1-3].

Actuation forces used in the RF-MEMS switches are representatively electrostatic, piezoelectric, electromagnetic, and thermoelastic. The electrostatic actuator is the leading candidate because of its simple structure, CMOS compatible process, and high generated force. In spite of these advantages, the RF-MEMS switches using the electrostatic actuator have disadvantages of relatively slow switching speeds over 10  $\mu$ s, high actuation voltages over 10 V, mechanical reliability, and larger footprint size than the semiconductor switches. They obstruct the RF-MEMS switches to be used in the wireless communication terminals. Low actuation voltage makes switching speed slow, on the other hand, a fast switching speed needs high actuation voltage [4-7]. The past reported works of lower actuation voltage than 10 V, and a laterally movable actuator, the response time is still over 10  $\mu$ s [8-12]. The other type of rotary actuator

was also reported [13]. The trade-off relation between the switching speed and the actuation voltage makes it difficult to solve undesirable actuation characteristics.

For low voltage actuation and fast response in RF-MEMS switches, it is effective to reduce the spring constant of membrane used for the actuator. However, lower mechanical restoring force due to the lower spring constant is the cause of a slower response time into a separated state between the electrodes. This has been a critical problem in the past reported RF-MEMS switches. A pull-up electrode approach above the membrane is one of solutions to this problem, but a complicated structure increases the number of processes and process cost. Vertical comb-drive approach is reported to achieve a fast pull-up response using a simple structure with two metal layers [14,15]. Lateral comb-drive actuators integrated in circuit are also reported, and actuation voltage is still over 10 V [16,17].

This chapter reveals that the laterally movable triple electrodes actuator embodied with a simple and low-cost one metal layer process is effective for a low voltage actuation and fast response in RF-MEMS switches.

## **3.2. Design**

### **3.2.1. Effect of Laterally Movable Triple Electrodes Actuator**

The schematic diagram of the switch as described in this chapter is shown in Figure 3.1a overview and Figure 3.1b cross-sectional view. In the on-state, actuation voltage is applied between the center electrode and left electrode and these two electrodes come into contact. The RF signal goes

through from the input port to the output port. In the off-state, the center electrode and right electrode come into contact and the RF signal goes through to the ground. The RF signal is shut, not to be transmitted to RF output port. An equivalent circuit of the switch is shown in Figure 3.1c. The series and shunt type switches can be expressed on one switch. The series switch consists of the center electrode and the left electrode connected to RF input port and RF output port, respectively. On the other hand, the shunt switch consists of the center electrode and the right electrode connected to RF input port and the ground. The series switch is closed, and the shunt switch is opened in the on-state. To reverse in the off-state, the connection to the ground enables high isolation in spite of a small gap between the electrodes on the series switch. The small gap makes the response time shorter at a low actuation voltage, because the electrostatic force depends inversely on the gap by the factor of 2.

The triple electrodes are allowed to move laterally by electrostatic forces in not only the on-state but also the off-state, thus the restoring spring force can be reduced. A spring constant of the electrodes small enough to reduce pull-in voltage must be chosen. According to an expression for fixed-fixed beam, the spring constant  $k$  of the electrodes depends on physical dimensions, residual stress, and intrinsic material stiffness, given by the following [18]:

$$k = 32Ew \left(\frac{t}{l}\right)^3 + 8\sigma(1 - \nu)w \left(\frac{t}{l}\right) \quad (3.1)$$

where  $w$ ,  $t$ , and  $l$  are width, thickness, and length, respectively;  $E$  is the Young's modulus;  $\nu$  is the Poisson's ratio; and  $\sigma$  is the residual stress of the movable electrodes. The length is effective in order to reduce the spring

constant because the spring constant depends inversely on the length by the factor of 3 in the case of low residual stress.

A comparison of simulated response time between the case of both sides of the electrodes movable and one side movable is shown in Figure 3.2a. The actuation characteristics are calculated with dynamic analysis equation described in the work of [19]. The calculation parameters are  $w = 2 \mu\text{m}$ ,  $t = 2 \mu\text{m}$ ,  $l = 300 \mu\text{m}$ , gap between electrodes  $g = 0.6 \mu\text{m}$ , and actuation voltage  $V = 7 \text{ V}$ . The response time is  $5 \mu\text{s}$  in the case of both electrodes movable, which is nearly 1.5 times shorter than  $7.4 \mu\text{s}$  in the case of one side movable. The travel distance of each electrode becomes half of the case of one side movable, this configuration is effective for a low voltage actuation and fast response. The simulated response time as a function of residual stress of the movable electrode is shown in Figure 3.2b. The residual stress is determined to be a practical value of material under  $\sigma = 100 \text{ MPa}$  tensile stress to achieve actuation a voltage of  $7 \text{ V}$  and a response time of  $5 \mu\text{s}$ . The residual stress was evaluated from the mechanical resonant frequency of the movable electrodes, measured by laser Doppler interferometer.

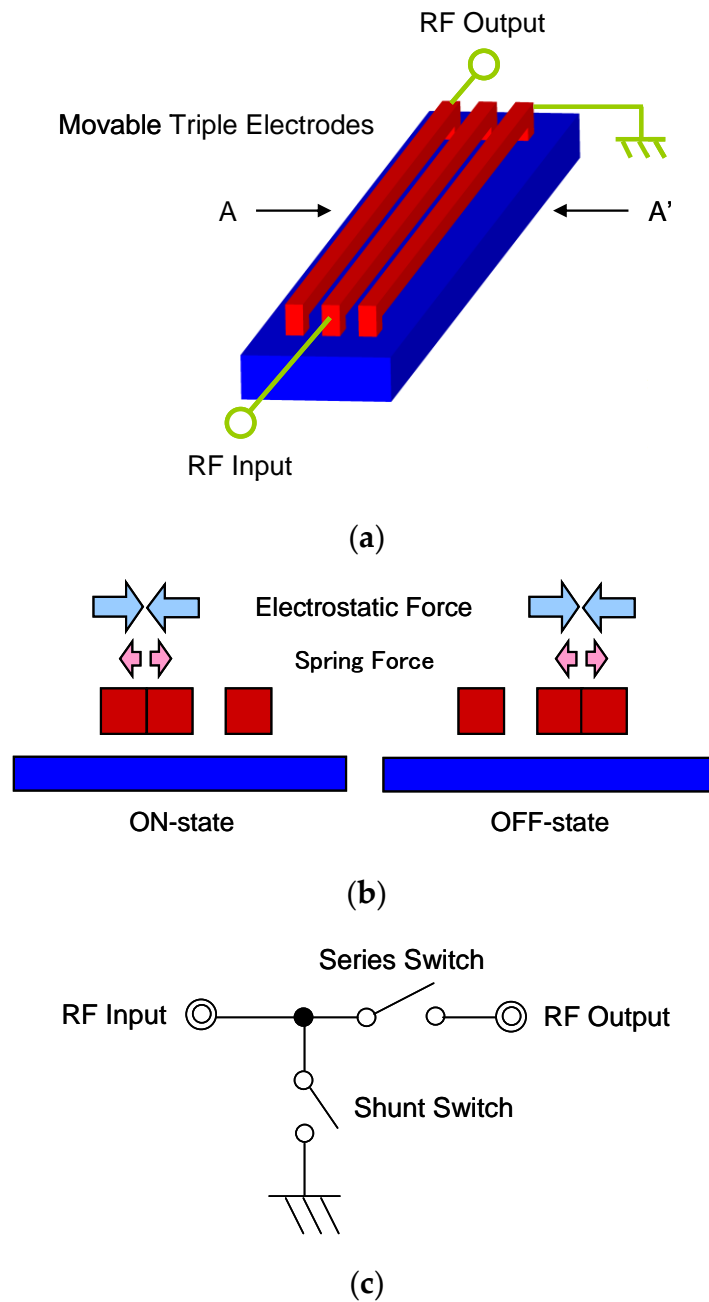
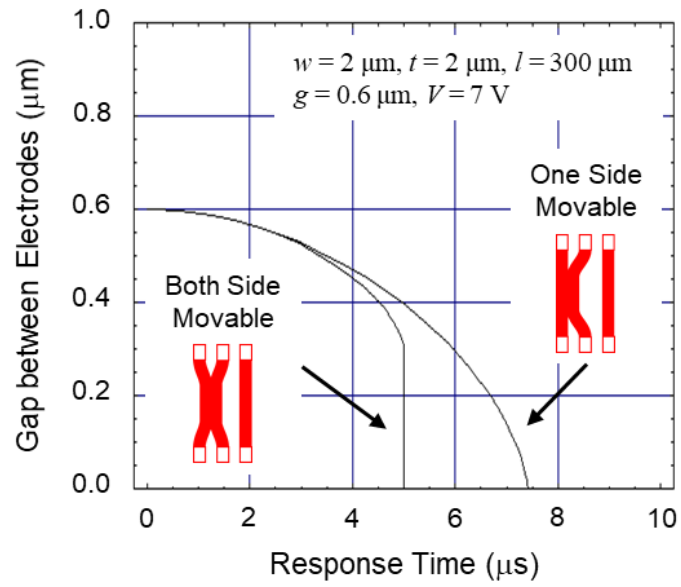
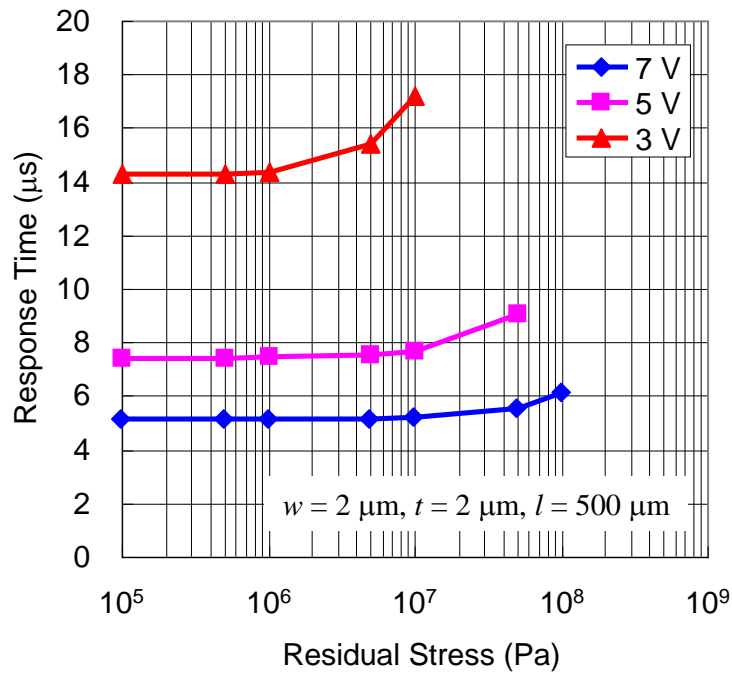


**Figure 3.1.** Schematic diagram of the RF-MEMS switch using laterally movable triple electrodes actuator: (a) overview; (b) cross-sectional view along A-A'; and (c) equivalent circuit.



(a)



(b)

**Figure 3.2.** (a) Comparison of simulated response time between case of both side of electrodes movable and one side movable; (b) simulated response time as a function of residual stress of movable electrode.

### 3.2.2. Movable Electrode as RF Transmission Line

Not only the actuation characteristics, but also the RF characteristic is essential to optimize the movable electrode dimension. The simulated response time and insertion loss as a function of length of the movable electrode are shown in Figure 3.3. An electromagnetic field analysis (Agilent Momentum) is used for the insertion loss simulation. The calculation parameters are  $w = 2 \mu\text{m}$ ,  $t = 2 \mu\text{m}$ ,  $g = 0.6 \mu\text{m}$ , and the dielectric material inserted between two signal lines is  $\text{Al}_2\text{O}_3$  (thickness  $t_d = 10 \text{ nm}$ , dielectric constant  $\epsilon_r = 10$ ). The insertion loss of the series switch depends on capacitance determined by lateral overlap area between the movable electrodes. If the length becomes longer, the insertion loss decreases as a result of the increase of the capacitance. The response time becomes shorter as a result of the decrease of the spring constant, according to Equation (3.1). Beyond a certain length, as the membrane gets longer, the insertion loss increases again as a result of the increased resistance of the electrodes. In this situation, the capacitive coupling loss is not more than the resistive loss. The geometry needs to satisfy both the actuation characteristics and the RF characteristics in order to optimize the movable electrode dimensions. The length of the movable membrane  $l$  was optimized to  $500 \mu\text{m}$ , at the same time minimizing the insertion loss from the transmission lines  $-0.22 \text{ dB}$  at  $5 \text{ GHz}$  and the response time  $5 \mu\text{s}$  at the actuation voltage of  $7 \text{ V}$ .

The simulated RF characteristics as a function of gap between electrodes of series shunt hybrid switches is shown in Figure 3.4a, which is done using a high frequency circuit simulator (Agilent ADS). The insertion loss is lower than  $-0.5 \text{ dB}$  and the isolation is higher than  $-30 \text{ dB}$ , including

the loss of the transmission lines from 1 to 5 GHz. The simulated response time as a function of gap between electrodes is shown in Figure 3.4b. The response time is shortened to 4  $\mu\text{s}$  at the higher actuation voltage 9 V in the case of the designed gap of 0.6  $\mu\text{m}$ .

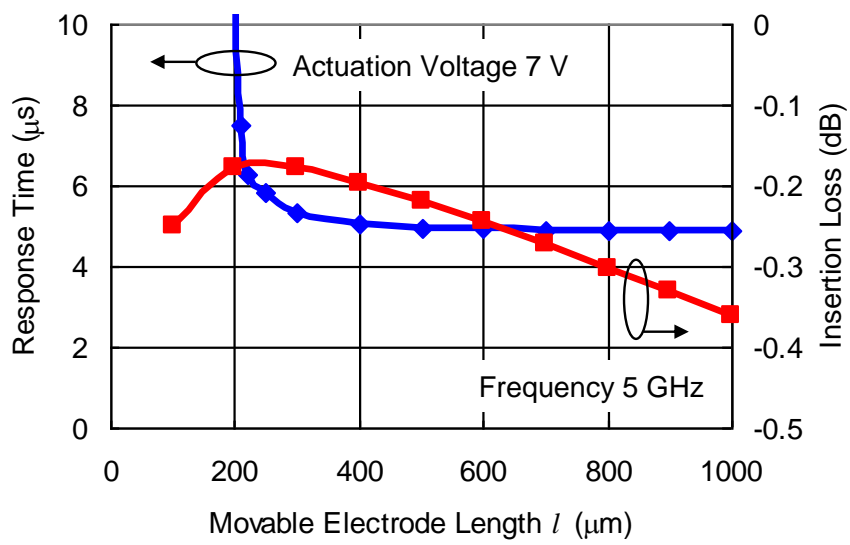
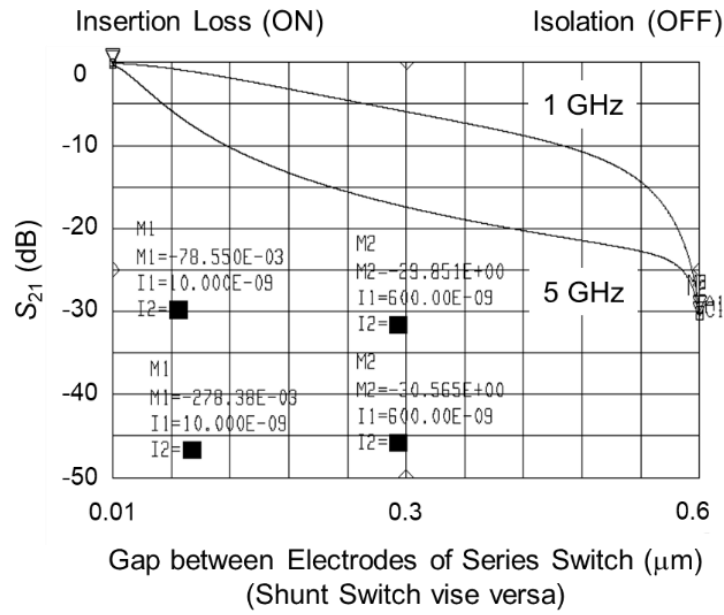
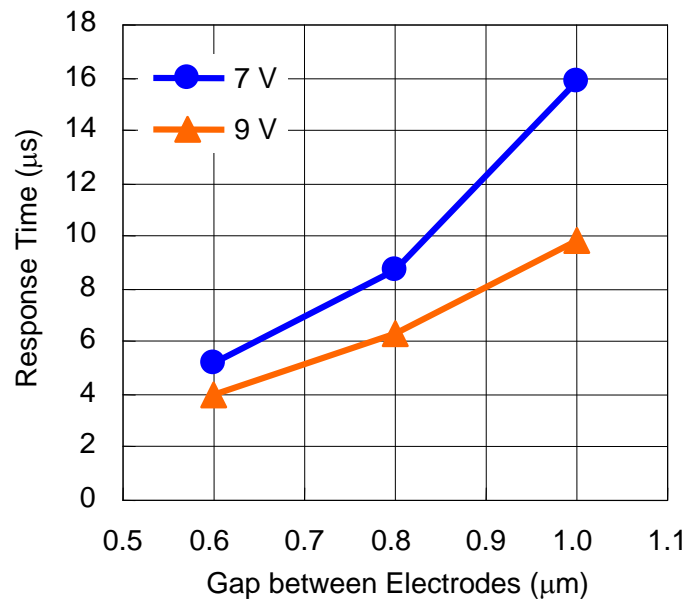


**Figure 3.3.** Simulated response time and insertion loss as a function of length of movable electrode.



(a)



(b)

**Figure 3.4.** (a) Simulated RF characteristics as a function of gap between electrodes of series shunt hybrid switches; (b) simulated response time as a function of gap between electrodes.

### 3.2.3. Summary of Design

The results of design predict that the movable triple electrodes actuator has a potential toward low voltage actuation and fast response in RF-MEMS switches. The designed specifications are summarized in Table 3.1.

**Table 3.1.** Designed specifications of movable triple electrodes actuator in RF-MEMS switches.

<b>Movable Electrodes</b>		
	Length ( $l$ )	500 $\mu\text{m}$
	Width ( $w$ )	2 $\mu\text{m}$
	Thickness ( $t$ )	2 $\mu\text{m}$
	Gap ( $g$ )	0.6 $\mu\text{m}$
	Actuation Voltage	7 V
	Response Time	5 $\mu\text{s}$
<b>RF Frequency</b>	<b>Insertion Loss</b>	<b>Isolation</b>
1 GHz	-0.3 dB	-30.1 dB
5 GHz	-0.5 dB	-30.8 dB
Gap ( $g$ )		
Series Switch (Shunt vise versa)	0.01 $\mu\text{m}$	0.6 $\mu\text{m}$

### 3.3. Fabrication

#### 3.3.1. Process Flow

The fabrication process flow for the switches is shown in Figure 3.5. The structures were fabricated using a simple, low-cost two-mask process. The switches were fabricated on the high-resistivity silicon substrate (2000-20,000  $\Omega\cdot\text{cm}$ ) with an isolation oxide layer. A photoresist was spin-coated and patterned to create a sacrificial layer. Post-bake with hotplate and DUV (deep ultraviolet) were implemented to smooth the edges of the photoresist. The movable triple electrodes were fabricated by sputtering 2  $\mu\text{m}$  aluminum alloy (Al-1%Si-0.5%Cu) and patterned. The low residual stress under  $\sigma = 100$  MPa tensile stress was achieved with low temperature Al sputtering below 200  $^{\circ}\text{C}$  to avoid thermal stress. The 0.6  $\mu\text{m}$  air gaps between the electrodes were patterned with photolithography using i-line stepper and etched using RIE. Thick photoresist was used in order to etch the thick aluminum layer. Finally, the sacrificial photoresist was removed using oxygen plasma to eliminate stiction of the beams. The aluminum electrodes are covered with  $\text{Al}_2\text{O}_3$  native oxide dielectric layer.

The stress simulation results using FEM (CoventorWare) are shown in Figure 3.6. The stress is concentrated to the support area because of the tensile stress of the fixed-fixed beams. It is revealed that the stress concentration can be decreased in case of smaller angle between the ground and the support using smooth edges of the photoresist formed with higher temperature post-bake. Structural breakdown was observed at the stress concentrated part in SEM images in Figure 3.6a. The angle between the

ground and the support 45 ° by 150 °C post-bake was not sufficient, the temperature of the post-bake was adjusted in order to make the optimal shape of the sacrificial photoresist, 30 ° by 180 °C post-bake. In order to avoid the stress concentration, wider supports were also effective. The triple electrodes structures were fabricated by the stress control in the beams and the supports.

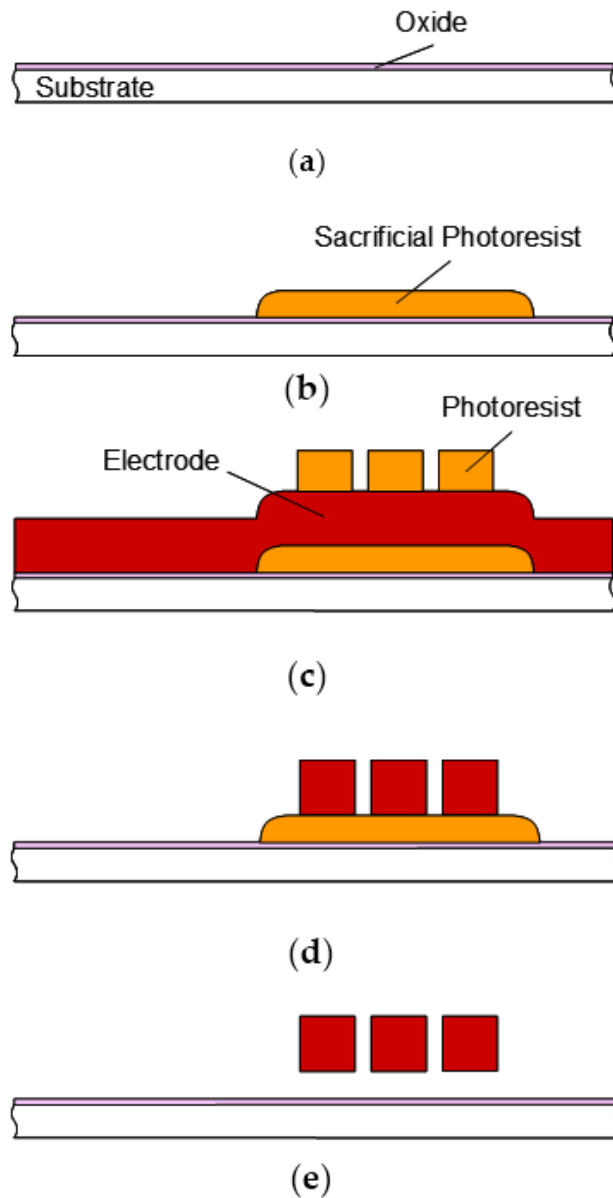


**Figure 3.5.** Fabrication process flow for sputtered-Al switch: (a) formation of isolation oxide on substrate; (b) formation of sacrificial photoresist; (c) Al deposition for electrodes, and photoresist formation; (d) Al etching; (e) release of electrodes as actuator.

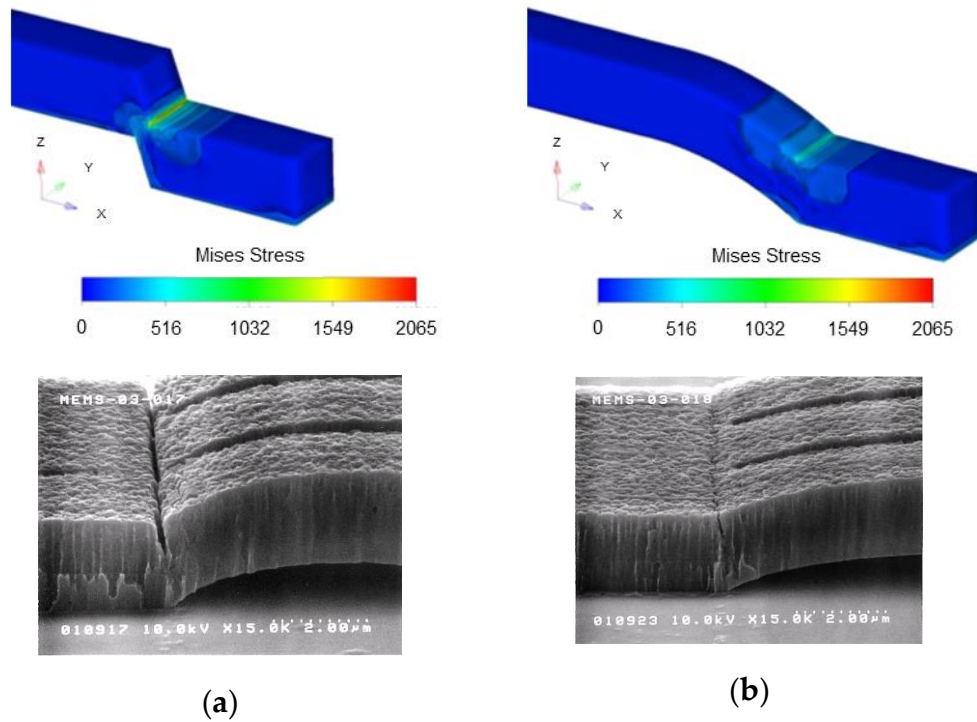
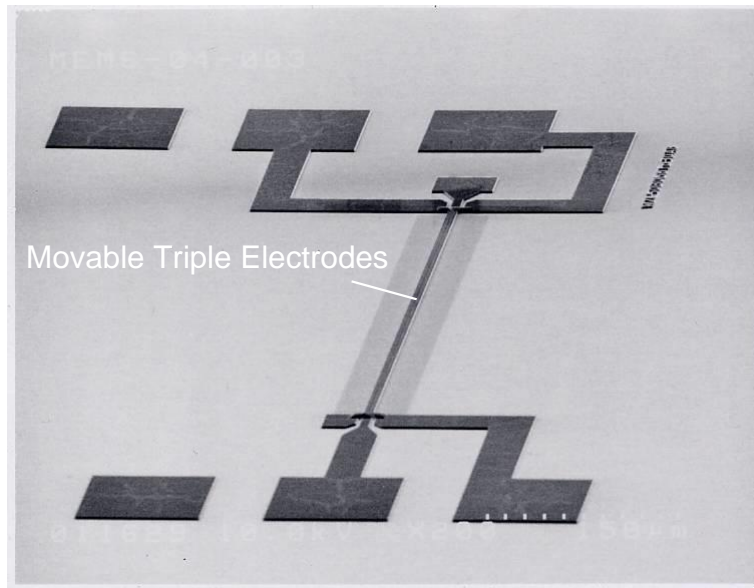


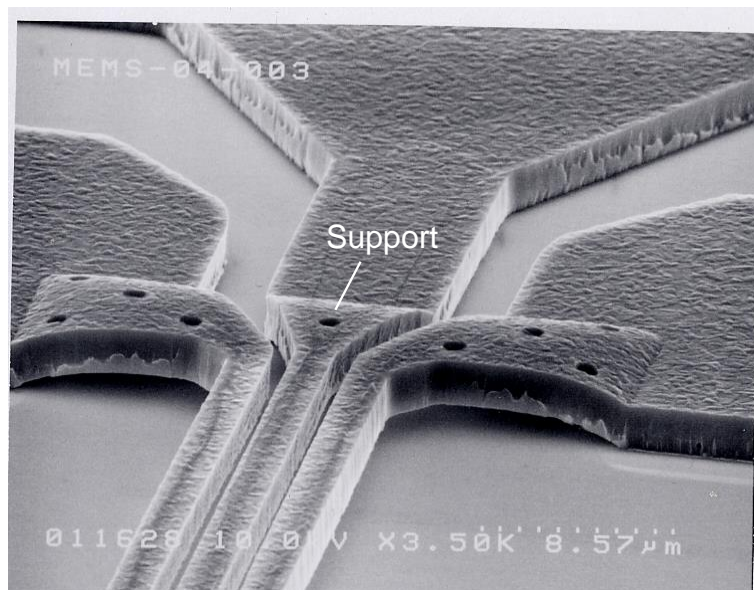
**Figure 3.6.** Simulated stress and SEM images of support area at post-bake temperature for sacrificial photoresist: (a) 150 °C; (b) 180 °C.

### 3.3.2. Structure Observation

SEM images of the fabricated switches are shown in Figure 3.7a overview and Figure 3.7b close-up of the support area. The laterally movable triple electrodes actuator for RF-MEMS switches reflected the geometry specifications shown in Table 3.1.



(a)



(b)

**Figure 3.7.** SEM images of fabricated switches: (a) overview; (b) close-up of support area.

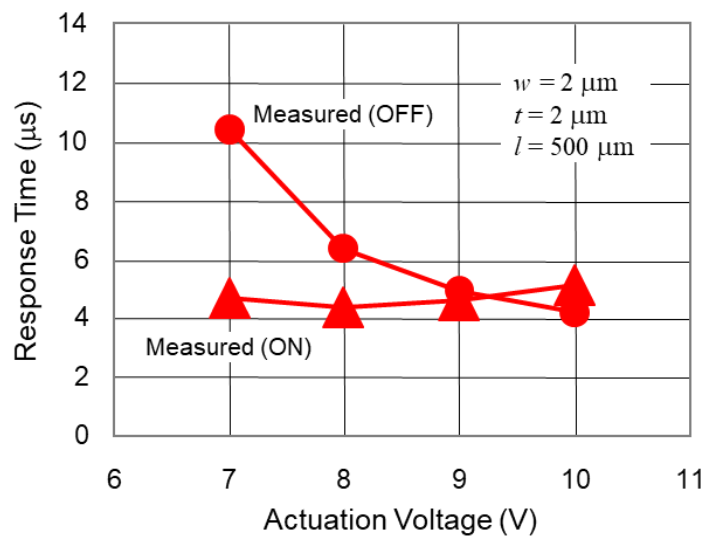
### 3.4. Measurement Result

The response time of the fabricated switches was measured using the control voltage applied to the center electrode with 1 kHz rectangular wave form. The applied control signals are summarized in Table 3.2. The high control signal means the actuation voltage, while the low one means the grounded 0 V. The bistable actuation consumes more power than monostable, but less than thermoelectric actuators [10,13]. The measured response time as a function of the actuation voltage is shown in Figure 3.8a. The response time and the actuation voltage were 4.9  $\mu\text{s}$  at 7 V in the on-state, which was in good agreement with the simulation. The characteristics in the off-state was 10.5  $\mu\text{s}$  at 7 V. A comparison with the simulation is shown in Figure 3.8b. A higher voltage than 9 V is necessary to achieve a response time of 5.0  $\mu\text{s}$ .

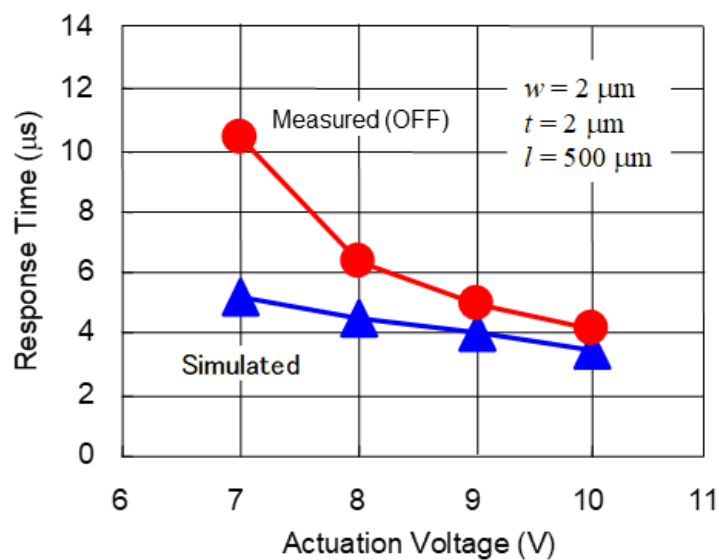
The reason for the deviation between the measured and the simulated actuation voltage in the off-state is considered to be larger gap between the center and the right electrodes. The measured gap using laser microscopy was around 0.8  $\mu\text{m}$ , which was 0.2  $\mu\text{m}$  larger than the geometry specifications caused by deformation of the electrodes as a result of stress distribution in asymmetric support structure. The actuation voltage of 9 V was necessary to achieve a response time of 5.0  $\mu\text{s}$  in the case of the gap between the electrodes of around 0.8  $\mu\text{m}$ , which was in agreement with the simulated results in Figure 3.4b. The measured RF signal as a function of time is shown in Figure 3.9. It was confirmed that the response time became shorter 4.2  $\mu\text{s}$  at actuation voltage 10 V on the shunt switch in the off-state.

**Table 3.2.** Applied control signals of movable triple electrodes actuator.

	Left Electrode	Center Electrode	Right Electrode
ON	High	Low	Low
OFF	High	High	Low

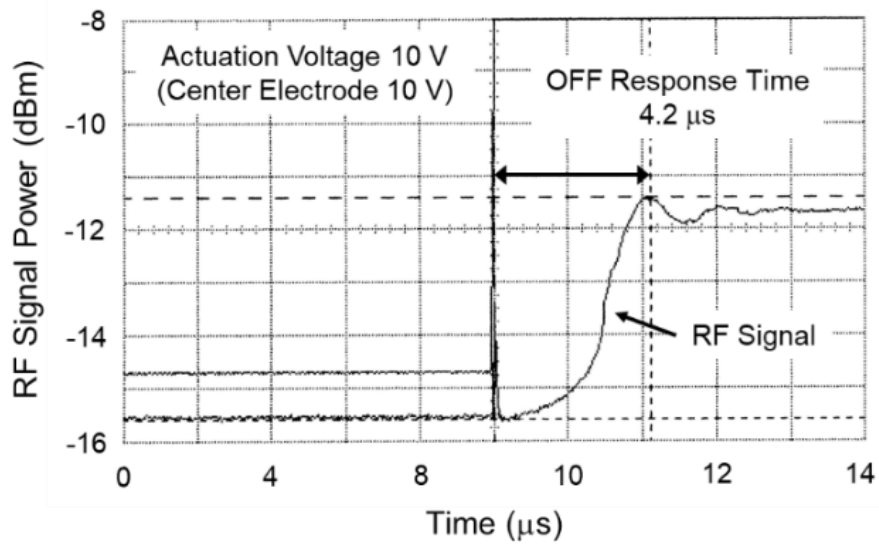


(a)

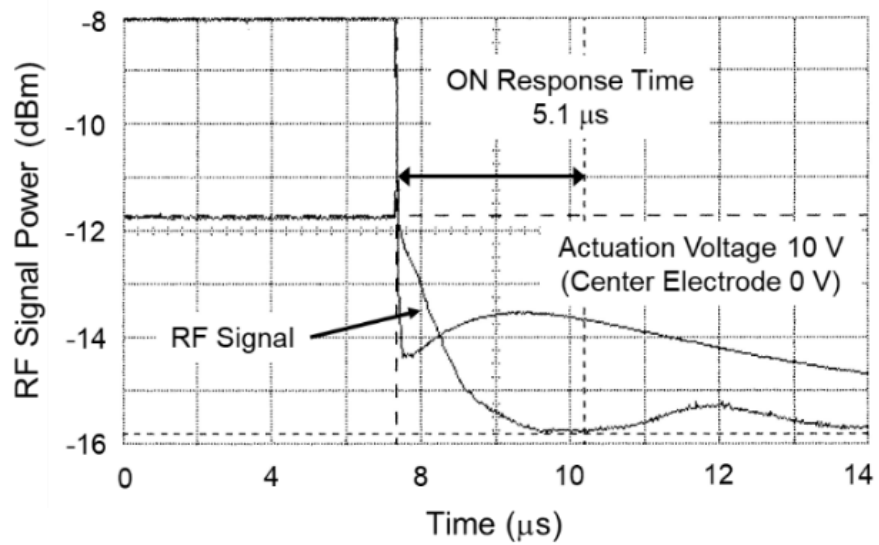


(b)

**Figure 3.8.** (a) Measured response time as a function of actuation voltage; (b) comparison with simulation in the off-state.



(a)



(b)

**Figure 3.9.** Measured RF signal as a function of time on shunt switch: (a) on-state; (b) off-state.

### 3.5. Discussion

In this chapter, the design, fabrication, and testing of laterally movable triple electrodes actuator in capacitive series shunt hybrid RF-MEMS switches for a low voltage actuation and fast response were described. The actuator allows all of the suspended beams to move laterally in two directions entirely by electrostatic forces. The structure was optimized considering the RF and mechanical characteristics. The switches were fabricated using a simple, low-cost two-mask process with sputtered aluminum as the structural material. The measured response time and the actuation voltage were  $5.0 \mu\text{s}$  and  $9 \text{ V}$ , respectively. The experimental results were in good agreement with the simulated actuation characteristics.

Consequently, it was revealed that the laterally movable triple electrodes actuator is effective toward the lower actuation voltage than  $10 \text{ V}$  and the faster response than  $10 \mu\text{s}$  in RF-MEMS switches. The advantage is summarized in comparison with reported works in Table 3.3.

For further work, improvement of roughness on the sidewall of the electrodes should be done for good electrical contact and RF characteristics. Mechanical fatigue should be also taken into consideration. A reliability test will be done to confirm that the bistable actuation is effective to avoid stiction of the electrodes.

One of the issues for commercialization is packaging technology for high reliability. A hermetic package is required in order to avoid aluminum oxidation and adhesion of the movable electrode due to humidity. In the case of vacuum, a chattering phenomenon occurs in which the movement of the movable electrode cannot be settled down because there is no air

viscosity. For this reason, it is preferable to replace with an inert gas such as nitrogen. The MEMS packaging technology is also developed with chip-level and wafer-level bonding technology.

It is expected that the laterally movable triple electrodes actuator advances RF-MEMS switches, switched capacitors, and MEMS devices in circuits for wireless sensor networks.

**Table 3.3.** Comparison of low voltage actuators in RF-MEMS switches.

	Ref. [8]	Ref. [9]	Ref. [10]	Ref. [11]	Ref. [12]	This Work
Actuator Type	Vertical Monostable ON: ES OFF: MR Au	Vertical Monostable ON: ES OFF: MR Au	Lateral Monostable ON: ET OFF: MR Poly-Si	Lateral Monostable ON: ES OFF: MR Si	Lateral Bistable ON: ES OFF: ES Si	Lateral Bistable ON: ES OFF: ES Al
Switch Type	Ohmic series	Capacitive shunt	Ohmic series	Ohmic series	Ohmic series	Capacitive series shunt hybrid
Actuation Voltage	0.5 V	4.8–6.2 V	2.5–3.5 V	15 V	57 V	9.0 V
Response Time	500 $\mu$ s	33–37 $\mu$ s	300 $\mu$ s	120 / 500 $\mu$ s	56 / 40 $\mu$ s	5.0 $\mu$ s
Footprint Size	1264 $\times$ 635 $\mu$ m <sup>2</sup> (Incl. pads)	300 $\times$ 180 $\mu$ m <sup>2</sup>	200 $\times$ 100 $\mu$ m <sup>2</sup>	2.55 $\times$ 2.39 mm <sup>2</sup>	1.4 $\times$ 1.4 mm <sup>2</sup>	550 $\times$ 50 $\mu$ m <sup>2</sup>
RF Frequency	3k–3 GHz	20–40 GHz	40–50 GHz	DC–10 GHz	DC–10 GHz	1–5 GHz

ES: Electrostatic, ET: Electrothermal, MR: Mechanical Restoring.

## References

1. Nguyen, C.T.-C.; Katehi, L.P.B.; Rebeiz, G.M. Micromachined devices for wireless communications. *Proc. IEEE* 1998, 86, 1756-1768.
2. Yao, J.J. RF MEMS from a device perspective. *J. Micromech. Microeng.* 2000, 10, R9-R38.
3. Tilmans, H.A.C.; De Raedt, W.; Beyne, E. MEMS for wireless communications: 'From RF-MEMS components to RF-MEMS-SiP'. *J. Micromech. Microeng.* 2003, 13, S139-S163.
4. Schlaak, H.F.; Arndt, F.; Hanke, M. Silicon-microrelay—A small signal relay with electrostatic actuator. In *Proceedings of the 45th Annual Int. Relay Conference, Lake Buena, FL, 23 July 1997*; pp. 10.1-10.7.
5. Pacheco, S.; Nguyen, C.T.; Katehi, L.P.B. Micromechanical electrostatic K-Band switches. *IEEE MTT-S Int. Microwave Symp. Dig.: Baltimore, MD, USA, 1998*; pp. 1569-1572.
6. Yao, Z.J.; Chen, S.; Eshelman, R.; Denniston, D.; Goldsmith, C.L. Micromachined low-loss microwave switches. *IEEE J. Microelectromech. Syst.* 1999, 8, 129-134.
7. Zavracky, P.M.; McGruer, N.E.; Morrison, R.H.; Potter, D. Microswitches and microrelays with a view toward microwave applications. *Int. J. RF Microwave Comput. Aided Eng.* 1999, 9, 338-347.
8. Attaran, A.; Rashidzadeh, R. Ultra low actuation voltage RF MEMS switch. *Micro Nano Syst. Lett.* 2015, 3, 7.
9. Shekhar, S.; Vinoy, K.J.; Ananthasuresh, G.K. Surface-micromachined capacitive RF switches with low actuation voltage and steady contact. *IEEE J. Microelectromech. Syst.* 2017, 26, 643-652.

10. Wang, Y.; Li, Z.; McCormick, D.T.; Tien, N.C. A low-voltage lateral MEMS switch with high RF performance. *IEEE J. Microelectromech. Syst.* 2004, 13, 902-911.
11. Kang, S.; Kim, H.C.; Chun, K. Single pole four throw RF MEMS switch with double stop comb drive. In *Proceedings of the 2008 IEEE 21st International Conference on Micro Electro Mechanical Systems, Tucson, AZ, USA, 13-17 January 2008*; pp. 1036-1039.
12. Wang, L.; Han, L.H.; Tang, J.; Huang Q. Laterally-actuated inside-driven RF MEMS switches fabricated by a SOG process. *J. Micromech. Microeng.* 2015, 25, 065007.
13. Ilkhechi, A.K.; Mirzajani, H.; Aghdam, E.N.; Ghavifekr, H.B. A novel SPDT rotary RF MEMS switch for low loss and power efficient signal routing. *IETE J. Res.* 2016, 2, 68-80.
14. Naito, Y.; Shimizu, N.; Hashimura, A.; Nakamura, K.; Nakanishi, Y. A low-cost vertical comb-drive approach to low voltage and fast response RF-MEMS switches. In *Proceedings of the 34th European Microwave Conference, Amsterdam, The Netherlands, 12-14 October 2004*; vol. 3, pp. 1149-1152.
15. Naito, Y.; Nakamura, K.; Onishi, K. RF-MEMS switching devices using vertical comb-drive actuation in the CMOS process. *J. Micromech. Microeng.* 2010, 20, 045001.
16. Okamoto, Y.; Mori, I.; Mita, Y. Demonstration of 0-30V comb-drive MEMS actuator by integrated switching circuit with post-mesa-isolated standard 5V CMOS transistors. In *Proceedings of the 2016 Symposium on Design, Test, Integration and Packaging of MEMS/MOEMS (DTIP), Budapest, Hungary, 30 May-2 June 2016*.

17. Nagai, T.; Hane, K. Silicon adiabatic waveguide coupler switch using lateral comb actuators. In Proceedings of the 2018 International Conference on Optical MEMS and Nanophotonics (OMN), Lausanne, Switzerland, 29 July-2 August 2018.
18. Rebeiz, G.M. Mechanical modeling of MEMS devices: Static analysis. In RF MEMS Theory, Design, and Technology; Wiley & Sons, Inc.: Hoboken, NJ, USA, 2003; Chapter 2, Section 2.1, p. 27, 9780471201694.
19. Muldavin, J.B.; Rebeiz, G.M. Nonlinear electro-mechanical modeling of MEMS switches. In Proceedings of the 2001 IEEE MTT-S International Microwave Symposium Digest (Cat. No.01CH37157), Phoenix, AZ, USA, 20-24 May 2001; pp. 2119-2122.

## Chapter 4. High-Q Torsional Mode Si Triangular Beam Resonators Encapsulated using SiGe Thin Film

### 4.1 Introduction and Research Review

Silicon-resonator based oscillators provide an attractive alternative to replace conventional frequency control devices and timing devices that are based on high quality factor ( $Q$ ) resonators such as quartz crystal, piezoelectric ceramic and SAW [1-4]. Quartz crystal resonators display high frequency stability but are difficult to be miniaturized and cannot offer an integrated solution. Silicon MEMS resonators on the other hand offer enhanced miniaturization, low susceptibility to shock and vibration, and higher integration over conventionally used quartz crystal resonators. Drawbacks of MEMS-based oscillators remain the poor temperature stability, low phase noise and limited frequency accuracy. MEMS-based oscillators therefore appear suited to non-critical timing applications and applications where the signal-to-noise ratios are less important.

High- $Q$  MEMS resonators with low motional resistance  $R_m$  and low DC (direct current) bias  $V_{dc}$  are advantageous to attain high frequency accuracy (and stability) of a reference oscillator with low power consumption (by the sustaining amplifier and the charge pump). A MEMS resonator operating in a wine-glass mode of vibration with a  $Q$ -factor of 161,000 and an  $R_m$  of 11.73 k $\Omega$  has been reported [1], but it requires a rather high DC bias of 7 V. Similar observations are made from the square-extensional mode resonator [3], which requires a DC bias of 100 V in order to obtain the low  $R_m$  of 4.47 k $\Omega$ .

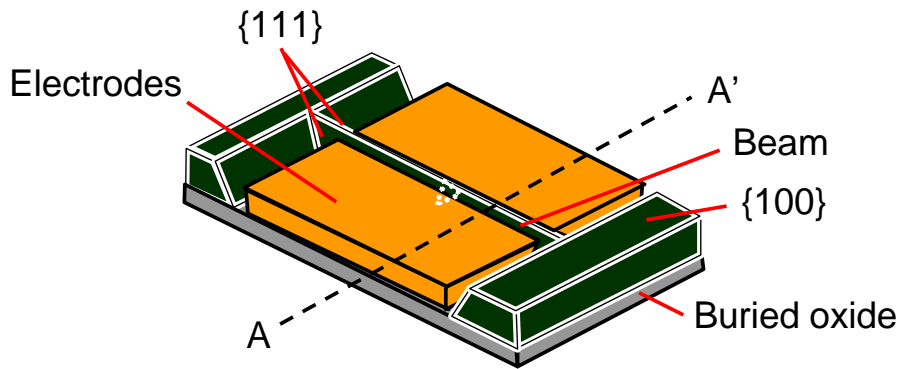
This chapter describes a novel silicon-based torsional mode resonator, offering superb performance characteristics, such as a  $Q$ -factor of around 220,000 for the torsional resonance at 20 MHz, a DC bias  $V_{dc}$  as low as 1 V associated with a motional resistance  $R_m$  of 11.9 k $\Omega$ . As illustrated in Figure 4.1, the resonator is built into the Si top layer of an SOI substrate, has a triangular-shaped cross-section and is operated in a torsional mode of vibration. Noteworthy is that the above characteristics are obtained from wafer-level vacuum packaged resonators [5]. The thin film packaging technology implements poly-SiGe (polycrystalline silicon-germanium) as the base material [6,7] complemented with a metal Al seal.

## 4.2 Design

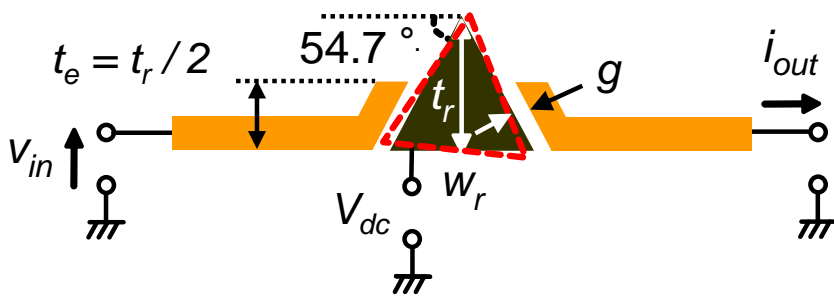
### 4.2.1. Torsional Mode Triangular Beam Resonator

Figure 4.1a shows a 3D view of the resonator, with a cross-sectional view in Figure 4.1b. The triangular beam displays the characteristic side angle of  $54.7^\circ$  resulting from the TMAH (tetramethylammonium hydroxide) anisotropic etching of the single crystalline Si. High quality single crystalline Si was chosen for the resonator body as it allows a high  $Q$ -factor in the end. Furthermore, in order not to comprise too much on the attainable  $Q$ -factor, a resonator operating in a torsional mode of vibration was chosen. Torsional modes are known for their relatively low anchor losses and for their lower squeeze film damping (as compared to flexural mode resonators [8]), thus allowing high  $Q$ -factors. The poly-Si electrodes for the electrostatic excitation and detection are positioned alongside the beam separated from the beam surface through a narrow gap  $g$ .

The simulated torsional mode resonant frequency of the triangular beam is shown Figure 4.2. Using FEM (CoventorWare), the fundamental torsional mode resonant frequency  $f_{\text{res}}$  is designed to be 20MHz resulting in a beam length  $l_r$  of 100  $\mu\text{m}$ , bottom width  $w_r$  of 4.25  $\mu\text{m}$  and a height  $t_r$  of 3  $\mu\text{m}$ . A harmonic analysis reveals that the displacement amplitude of the fundamental torsional mode displays a maximum when the electrodes are aligned along the {111} side-plane of the beam with a thickness  $t_e$  that equals half the beam height  $t_r$ . Therefore, by proper positioning of the electrodes, the transduction factor for the electrostatic sense and actuation (being proportional to the change in capacitance per unit displacement  $dC/dx$ ), and thus the motional resistance  $R_m$ , is optimized. The designed specifications are summarized in Table 4.1.

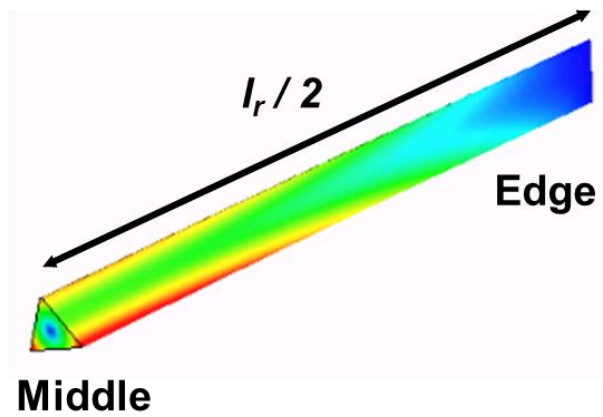


(a)

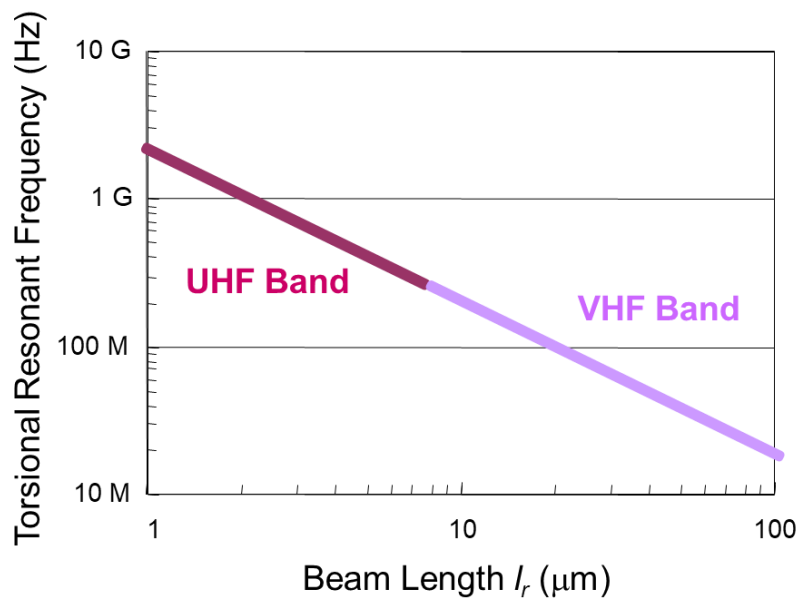


(b)

**Figure 4.1.** Schematic diagram of the torsional mode triangular beam resonator operated in a two-port configuration: (a) 3D view; (b) cross-sectional view along A-A' in (a).



(a)



(b)

**Figure 4.2.** Simulated torsional mode resonant frequency of triangular beam: (a) FEM model; (b) resonant frequency as a function of beam length.

**Table 4.1.** Designed specifications of torsional mode triangular beam in MEMS resonators.

<b>Torsional Mode Triangular Beam Resonator</b>	
Length ( $l_r$ )	100 $\mu\text{m}$
Width ( $w_r$ )	4.2 $\mu\text{m}$
Thickness ( $t_r$ )	3.0 $\mu\text{m}$
Electrode Height ( $t_e$ )	1.5 $\mu\text{m}$
Gap ( $g$ )	130 nm
1st Order Resonant Frequency ( $f_{\text{res}}$ )	20 MHz

#### 4.2.2 Wafer-level Thin Film Package

The  $Q$ -factor as a function of external pressure measured on an unsealed resonator is shown in Figure 4.3. The ambient gas is  $\text{N}_2$ , and the temperature is 25 °C. The  $Q$ -factor depends on the ambient pressure and starts to decrease above a critical pressure  $P_{\text{crit}}$  of 10 Pa, due to viscous and squeeze film damping effects. Therefore, to minimize these losses and to achieve a high- $Q$ , vacuum encapsulation of the resonator in a hermetically sealed environment is required. Thin film encapsulation using a monolithic fabrication process with the MEMS provides such a vacuum packaging solution. In this case, a 4  $\mu\text{m}$  thick impermeable (apart from the release

holes) SiGe thin film is used for the base capping layer. The in-plane size of the cavity together with the thickness of the thin film cap are dimensioned such that the thin film package offers sufficient strength against transfer molding pressures of at least 10 MPa. The inner pressure  $P_{inn}$  of the cavity is determined by the sealing method used [9-12]. In this work, sputter deposited Al at an ambient pressure as low as 1 Pa (Ar) for the sealing layer was used (*e.g.*, as illustrated in Figure 4.4d).

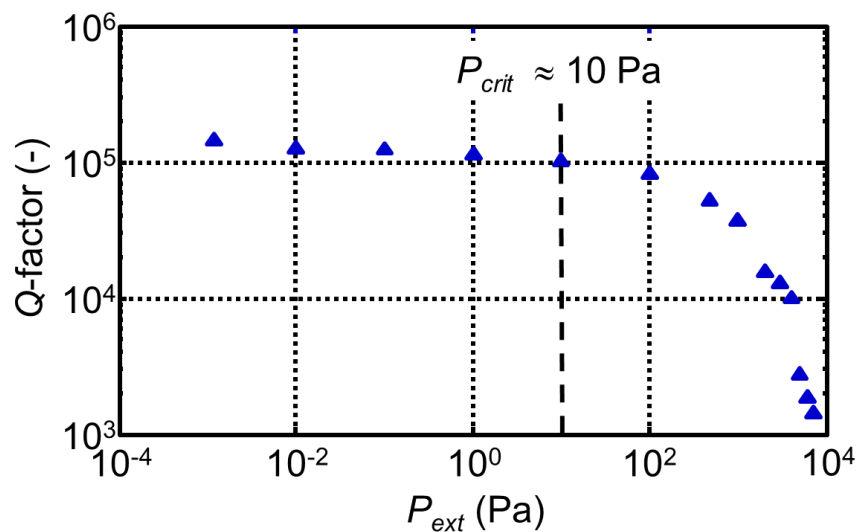


**Figure 4.3.** Q-factor as a function of external pressure measured on unsealed resonator.

### 4.3. Fabrication

The fabrication process flow of the encapsulated resonator is depicted in Figure 4.4. Silicon nitride is first patterned as a masking layer for the beam and the anchor on the SOI wafer along the  $\langle 110 \rangle$  orientation. An anisotropic etch in TMAH wet solution exposes the inclined  $\{111\}$  planes of the triangular shaped beam. A thin (130 nm) sacrificial silicon oxide layer is grown along the sides of the beam and defines the air gaps later on. The poly-Si layer for the electrodes is next deposited. Lithography at the top of the triangular beam is implemented to protrude the beam apex, and the poly-Si layer at the top of the beam is removed. The poly-Si electrodes on top of the BOX (buried oxide) are patterned.

Following the SiGe-based thin film encapsulation process, the sacrificial layer and the BOX layer underneath the beam are removed using vapor HF, and next, sputter deposited Al is used to seal the cavity at a pressure of 1 Pa. Finally, the Al layer as well as the isolation trenches in the poly-SiGe are etched to form the bonding pads.

Figure 4.5 shows a cross-sectional SEM of a fabricated packaged resonator.

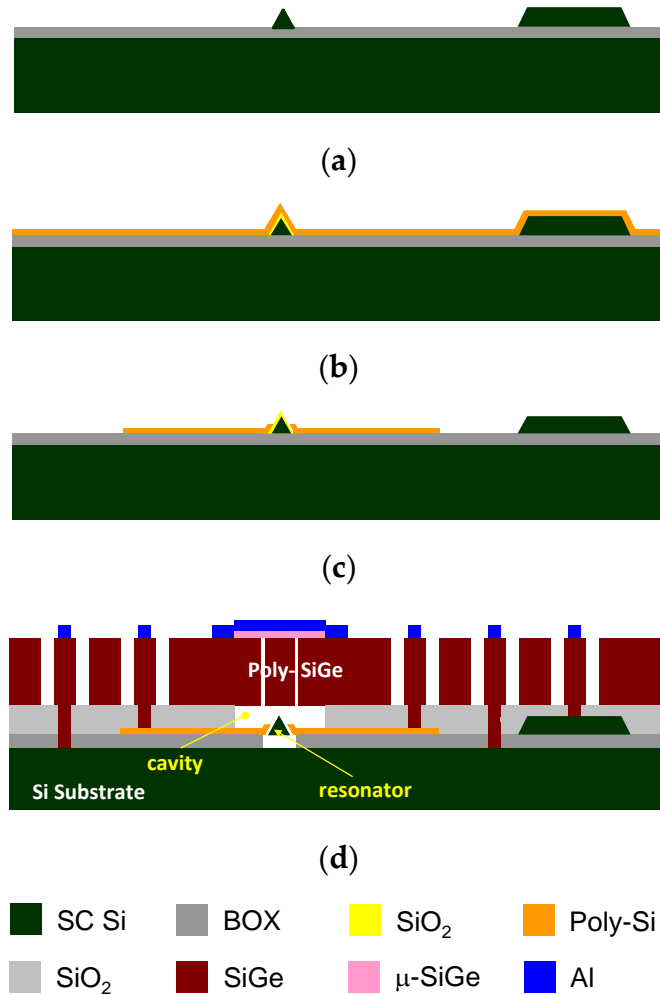


**Figure 4.4.** Fabrication process flow of the SOI-based triangular beam resonator encapsulated using thin film SiGe: (a) SOI substrate; TMAH anisotropic etch of triangular beam resonator; (b) deposition of 130 nm SiO<sub>2</sub> (sacrificial layer) and poly-Si (electrodes); (c) patterning of poly-Si (to protrude the beam apex, and to define the electrodes); (d) thin film (SiGe) encapsulation and sealing with Al (sputtered at 1 Pa Ar pressure).

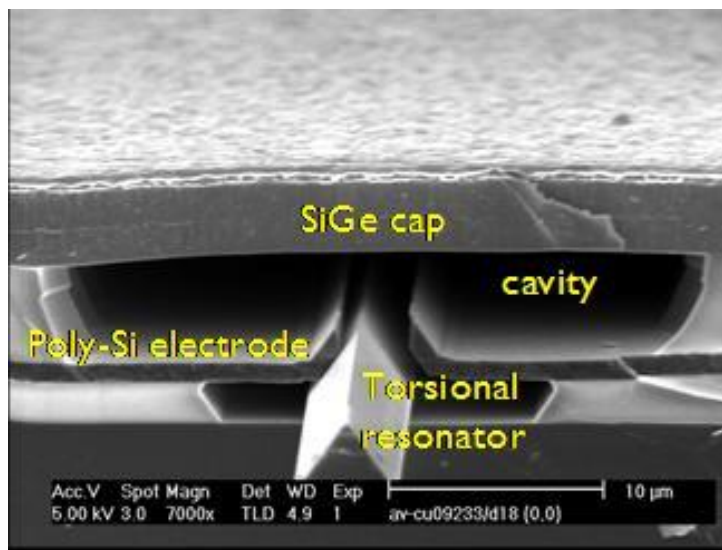


**Figure 4.5.** SEM image of cross-sectional view of fabricated triangular shaped, thin-film packaged resonators.

#### 4.4. Measurement Result

The frequency response ( $S_{21}$  parameter) of the encapsulated resonator, configured as a two-port (see Figure 4.1b), was measured under atmospheric pressure and is shown in Figure 4.6. At the resonance frequency of 19.4 MHz, a  $Q$ -factor was extracted of 220,201 implying a frequency- $Q$  product  $f_{\text{res}}Q$  of  $4.3 \times 10^{12}$ . The DC bias  $V_{\text{dc}}$  was as low as 1 V associated with a motional resistance  $R_m$  of 11.92 k $\Omega$ . Hermetic thin film encapsulation was revealed with an inner cavity pressure  $P_{\text{inn}}$  below the critical pressure  $P_{\text{crit}}$  of 10 Pa, which was obtained from measurements on leaky encapsulated resonators (with the sole intention to measure  $Q$  as a function of pressure).

The low  $R_m$  and low  $V_{\text{dc}}$  are a result of the high- $Q$  and the narrow gap  $g$  of 130 nm as expressed by the following proportionality:  $R_m V_{\text{dc}}^2 \propto g^4/(QA)$ , where  $A$  indicates the overlap area between the beam and the electrode.

The measured  $Q$ -factor turned out to be stable for over 4,000 hours at atmospheric pressure and at 25 °C (see Figure 4.7). A temperature coefficient of frequency TCf of -25 ppm/°C was extracted from the resonant frequency shift over a wide temperature range of -40 to +140°C in Figure 4.8, which is consistent with about half of the intrinsic temperature coefficient of the Young's modulus TCE of Si [13]. The measured high linearity of the TCf enables temperature compensation, eventually leading to a much lower TCf, using appropriate circuitry at a wider temperature range of -40 to +140 °C.

The resonator showed  $-0.4\%$   $Q$ -factor change for  $1^\circ\text{C}$  of temperature change. The  $Q$ -factor was kept over 100,000 for the whole temperature range (see Figure 4.9).

Operation of a CMOS-based oscillator using the MEMS torsional resonator (with  $g = 250\text{ nm}$ ,  $V_{\text{dc}} = 8\text{ V}$  as a demonstrator) as the frequency determining element was demonstrated (see Figure 4.10).

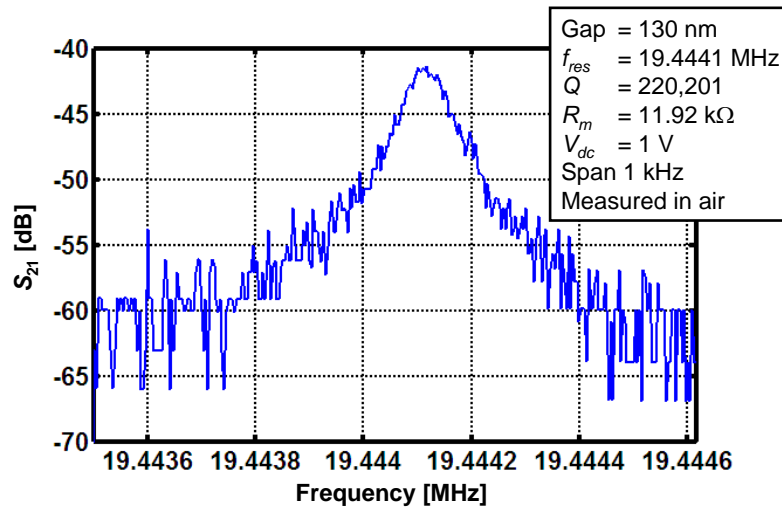


**Figure 4.6.** Measured RF transmission as a function of frequency of the SiGe encapsulated resonator.

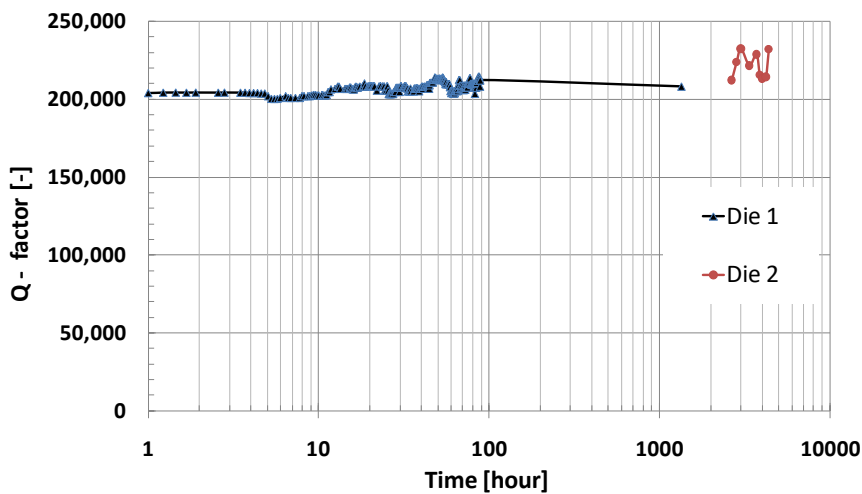


**Figure 4.7.** Measured  $Q$ -factor of two packaged resonators as a function of time. Measurements are done at 1 bar  $N_2$ , 25 °C. The  $Q$  value does not show noticeable change for over 4,000 hours. The Die 1 got accidentally broken (scratched by the probes) after 2000 hours of testing and therefore a swap was made to Die 2 located on the same wafer.

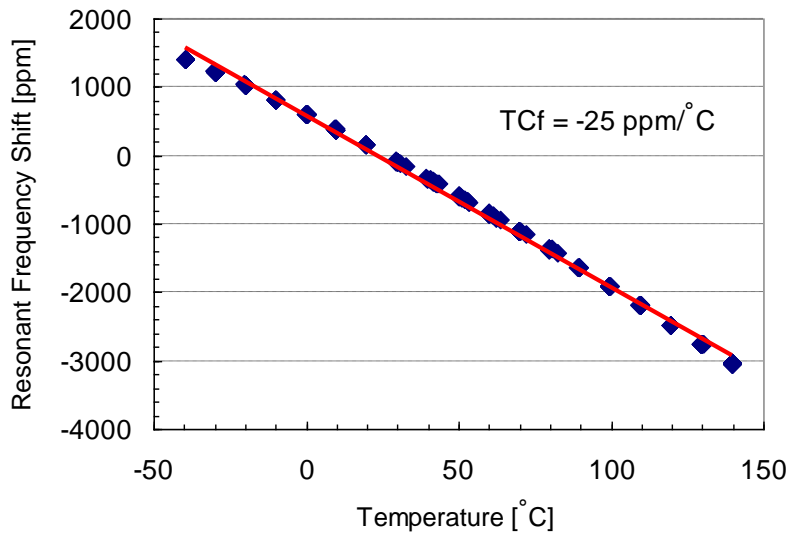


**Figure 4.8.** Measured relative resonant frequency shift ( $\Delta f_{\text{res}}/f_{\text{res}}$ ) as a function of temperature.

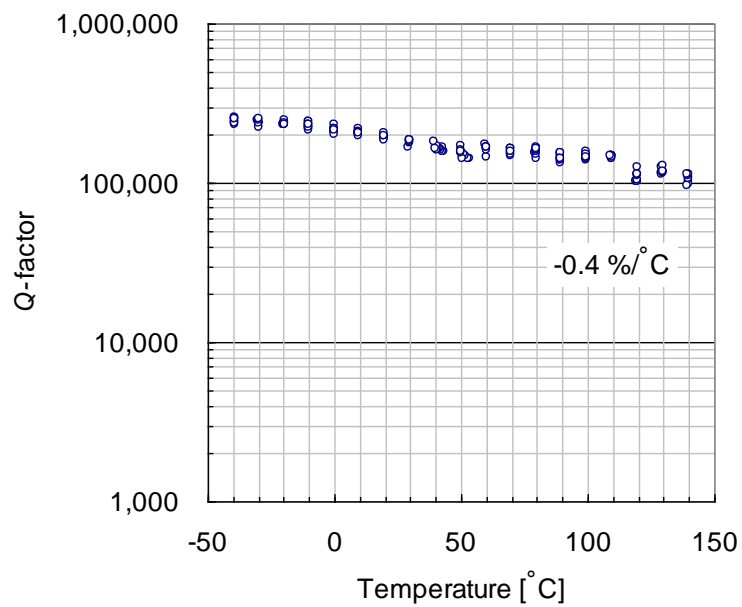


**Figure 4.9.** Measured  $Q$ -factor as a function of temperature.

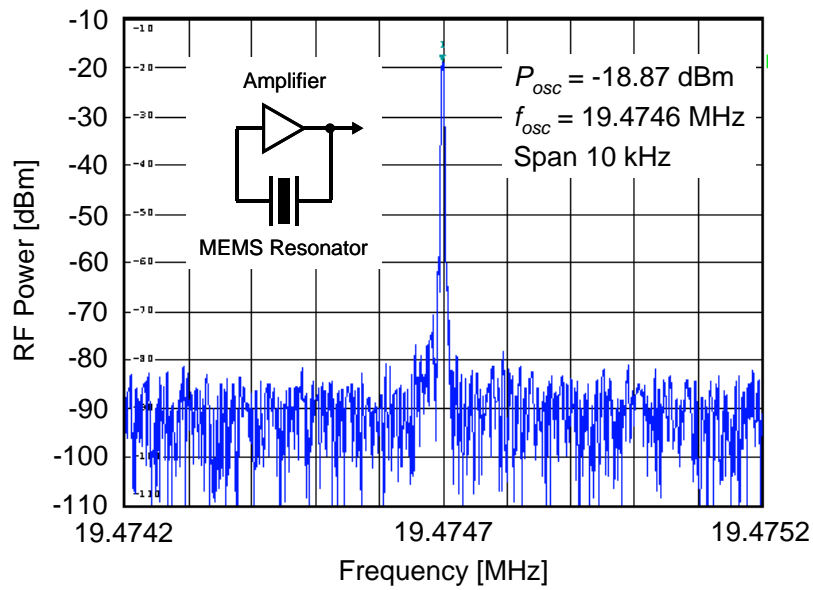


**Figure 4.10.** Measured RF power as a function of frequency on a fabricated CMOS-based oscillator using the MEMS torsional resonator (with  $g = 250$  nm and  $V_{dc} = 8$  V as a demonstrator) as the frequency determining element.

## 4.5. Discussion

In this chapter, novel torsional-mode single crystalline silicon triangular beam resonators, vacuum encapsulated using a thin SiGe film and sealed with Al at 1 Pa have been realized and resonance was demonstrated displaying a stable high- $Q$  (of around 220,000) with a low DC bias (1 V) and low motional resistance ( $< 12 \text{ k}\Omega$ ).

The triangular shaped beam was realized by an anisotropic etch of Si on SOI wafer. A  $4 \mu\text{m}$  thick SiGe thin film was used for the base capping layer such that the thin film package offers sufficient strength against transfer molding pressures of at least 10 MPa. Sputter deposited Al is used to seal the cavity at a pressure of 1 Pa.

The fundamental torsional mode resonance showed a  $Q$ -factor of 220,201 at  $f_{\text{res}} = 19.4 \text{ MHz}$ , a  $f_{\text{res}}Q$  product of  $4.3 \times 10^{12}$  (at DC bias  $V_{\text{dc}} = 1 \text{ V}$ ). A motional resistance  $R_m$  of  $11.92 \text{ k}\Omega$  was extracted from the transmission  $S_{21}$ .

The  $Q$  value did not show noticeable change for over 4,000 hours. TCf of  $-25 \text{ ppm}/^\circ\text{C}$  was extracted for the temperature range of  $-40$  to  $+140 \text{ }^\circ\text{C}$ , which is close to the expected half of the temperature coefficient of the Young's modulus TCE of Si. The resonator showed about  $-0.4 \%$   $Q$ -factor change for  $1 \text{ }^\circ\text{C}$  of temperature change. The  $Q$ -factor was kept above 100,000 in the temperature range of  $-40$  to  $+140 \text{ }^\circ\text{C}$ .

A fabricated CMOS-based oscillator using the MEMS torsional resonator (with  $g = 250 \text{ nm}$  and  $V_{\text{dc}} = 8 \text{ V}$ ) was also demonstrated as the frequency determining element.

One of the issues for practical use is a temperature compensation circuit. The resonators are necessary to be controlled by the driving voltage so that a constant frequency is oscillated since the resonant frequency changes with temperature. The temperature compensation control can be performed relatively easily because of the linear temperature characteristics. It is necessary to develop a driving circuits optimized to the MEMS devices.

Such high- $Q$  MEMS resonators with low  $R_m$  and low  $V_{dc}$  turn out to be advantageous to attain high frequency accuracy of a reference oscillator with a low power consumption.

## References

1. Nguyen, C.T.-C. MEMS technology for timing and frequency control. *IEEE Transactions on Ultrasonics, Ferroelectrics, and Frequency Control* 2007, 54, 251-270.
2. SiTime. Available online: <https://www.sitime.com> (accessed on 10 May 2019).
3. Kaajakari, V.; Mattila, T.; Oja, A.; Kiihamäki, J.; Seppä, H. Square-extensional mode single-crystal silicon micromechanical resonator for low-phase-noise oscillator applications. *IEEE Electron Device Letters* 2004, 25, 173-175.
4. van Beek, J.T.M.; Puers, R. A review of MEMS oscillators for frequency reference and timing applications. *J. Micromech. Microeng.* 2012, 22, 013001.
5. Kim, B.; Candler, R.N.; Melamud, R.; Hopcroft, M.A.; Yoneoka, S.; Lee, H.K.; Agarwal, M.; Chandorkar, S.A.; Yama, G.; Kenny, T.W. Hermeticity and diffusion investigation in polysilicon film encapsulation for microelectromechanical systems. *J. Applied Physics* 2009, 105, 013514.
6. Witvrouw, A.; Gromova, M.; Mehta, A.; Sedky, S.; De Moor, P.; Baert, K.; Van Hoof, C. Poly-SiGe, a superb material for MEMS. *Material Research Society Proceedings* 2004, 782, 25-36.
7. Franke, A.E.; Heck, J.M.; King, T.; Howe R.T. Polycrystalline silicon-germanium films for integrated microsystems. *Journal of Microelectromechanical Systems* 2003, 12, 160-171.

8. Christopher, P.; Green, P.; Sader, J.E. Torsional frequency response of cantilever beams immersed in viscous fluids with applications to the atomic force microscope. *Journal of Applied Physics* 2002, 92, 6262-6274.
9. Höchst, A.; Scheuerer, R.; Stahl, H.; Fischer, F.; Metzger, L.; Reichenbach, R.; Lärmier, F.; Kronmüller, S.; Watcham, S.; Rusu, C.; Witvrouw, A.; Gunn, R. Stable thin film encapsulation of acceleration sensors using polycrystalline silicon as sacrificial and encapsulation layer. *Sensors and Actuators A* 2004, 114, 355-361.
10. Verheijden, G.J.A.M.; Koops, G.E.J.; Phan, K.L.; van Beek, J.T.M. Wafer level encapsulation technology for MEMS devices using an HF-permeable PECVD SiOC capping layer. *IEEE International Conference on Micro Electro Mechanical Systems (MEMS)*, Tucson, AZ, USA, 13-17 January 2008; pp. 798-801.
11. Rajaraman, V.; Pakula, L.S.; Pham, H.T.M.; Sarro, P.M.; French, P.J. Robust wafer-level thin-film encapsulation of microstructures using low stress PECVD silicon carbide. *IEEE International Conference on Micro Electro Mechanical Systems (MEMS)*, Sorrento, Italy, 25-29 January 2009; pp. 140-143.
12. Yoneoka, S.; Qu, Y.Q.; Wang, S.; Messana, M.W.; Graham, A.B.; Salvia, J.; Kim, B.; Melamud, R.; Bahl, G.; Kenny, T.W. High-cycle fatigue experiments of single crystal silicon in an oxygen-free environment. *IEEE International Conference on Micro Electro Mechanical Systems (MEMS)*, Wanchai, Hong Kong, China, 24-28 January 2010; pp. 224-227.
13. Samarao, A.K.; Casinovi, G.; Ayazi, F. Passive TCF compensation in high Q silicon micromechanical resonators. *IEEE International Conference on Micro Electro Mechanical Systems (MEMS)*, Wanchai, Hong Kong, China, 24-28 January 2010; pp. 116-119.



## **Chapter 5. Electrostatic MEMS Vibration Energy Harvesters inside of Tire Treads**

### **5.1. Introduction and Research Review**

In order to improve the driving safety of automobiles, the requirements of TPMS (tire pressure monitoring systems) have advanced worldwide, starting with the United States and Europe. A tire sensor with the TPMS inside of tire tread enables gathering information of the road surface and tires for the detection of the degree of slippage. It is possible to control the attitude of the vehicle safely and comfortably. The tire sensor consists of not only a pressure sensor, but also an acceleration sensor and a temperature sensor, which improves the detection accuracy by analyzing the multifaceted data at a high frequency. It is necessary to supply stable power to the tire sensor during the life of tire because replacement of the power supply is not acceptable in consideration of user convenience and the reduction of cost.

As a power source, the battery capacity is insufficient to be applied here. For this reason, we tried to apply environmental power harvesters, which convert energy in the environment into electric energy. The environmental power harvesters include photovoltaic and thermoelectric types, but they are inappropriate because there is no light source or heat source inside of a tire. On the other hand, a vibration energy harvester could recover the power demand of the tire sensor since vibration energy is abundant inside of the tire [1,2].

An electrostatic vibration energy harvester is one of the expected candidates in power generation methods because the power output density

of the piezoelectric type or electromagnetic type is relatively low, and the device size becomes large. The electrostatic type needs an external voltage source to apply potential on electrodes for electric field generation [3]. An electrical charge holding an electret can be used as an internal voltage source of an electrostatic type. The electret vibration energy harvesters are classified mainly as the in-plane overlapping type [4] and the out-of-plane gap-closing type [5]. In the former type, the electrets displace in parallel to output electrodes in-plane. Methods for enhancement of accumulated charges on the output electrodes are reported: a higher electret potential using polymer electret [6], an inorganic insulator  $\text{SiO}_2/\text{Si}_3\text{N}_4$ -laminated film in a cost-effective CMOS/MEMS production line [7], an increased dielectric constant using ferroelectrics [8] and liquid crystals [9], an opposite-charged electret [10], and a potassium ion electret [11]. Structural optimization is also reported, a smaller air gap between electrets and output electrodes [12], and a mechanical nonlinearity with a spring stopper [13,14]. In most of these works, vibration energy harvesters are evaluated under sinusoidal vibration, which rarely exists in the real environment from the application point of view. Stochastic noise-like vibration tests are reported in the experimental environment [15,16].

For the TPMS and the tire sensors, electret vibration energy harvesters have to be evaluated considering the real impact vibration inside of the tire tread. The previously reported output power was  $4.5 \mu\text{W}$  in the case of PSD (power spectral density) of impact vibration acceleration of  $7.3 \times 10^{-2} \text{ g}^2 \cdot \text{Hz}^{-1}$  at a traveling speed of 50 km/h, and a mechanical resonance frequency of the harvester of 550 Hz [2]. In this chapter, an order of magnitude higher output power in spite of an order of magnitude lower PSD is presented. It is revealed that the higher resonance frequency of the

harvester adjusted within the frequency band of low PSD is effective for high efficiency harvest impact vibration energy. Output power from the harvester of a resonance frequency of 1.2 kHz reached 60  $\mu$ W in the case of PSD  $5.0 \times 10^{-3} \text{ g}^2 \cdot \text{Hz}^{-1}$  at a traveling speed of 60 km/h.

## 5.2. Design

### 5.2.1. Basic Concept of an Electrostatic MEMS Vibration Energy Harvester

A schematic cross-sectional view of the electret vibration energy harvester is shown in Figure 5.1. Three substrates are stacked and bonded together. A mechanical resonator is provided on the intermediate substrate, and the proof mass and spring are collectively formed by etching the Si substrate. A stacked film of  $\text{SiO}_2/\text{Si}_3\text{N}_4$  as an electret material is deposited on the corrugated structure of the proof mass and charged to a predetermined potential by a corona discharger. Al output electrodes are made on the lower substrate, which is used to extract generated electricity.

A design concept of the Si spring is the adjustment to a higher mechanical resonance frequency within the frequency band of PSD of the impact vibration acceleration inside of the tire tread, which enables harvesting more power at a high frequency. The PSD of impact vibration acceleration inside of the tire tread in the case of a traveling speed of 60 km/h is shown in Figure 5.2 [7]. The PSD in the tangential direction X of a circular tire is low from  $5.0 \times 10^{-3} \text{ g}^2 \cdot \text{Hz}^{-1}$  -  $1.0 \times 10^{-2} \text{ g}^2 \cdot \text{Hz}^{-1}$  at 250 Hz - 1.5 kHz. The resonance frequency of the Si spring is adjusted to a relatively high frequency at 1.2 kHz, which is also an advantage to make the Si spring small and rigid against the impact vibration.

The Si proof mass moves because of resonance under external vibration (sinusoidal vibration or impact vibration). Electric fields formed by charges stored in the electret induce charges at the facing output electrodes [17]. The proof mass displaces parallel to the direction in which strip-shaped output electrodes are arranged. The amount of charges on the output electrode is increased or decreased in response to the change of the electric fields. As a result, alternating current flows in the load circuit connected between the two output electrodes.

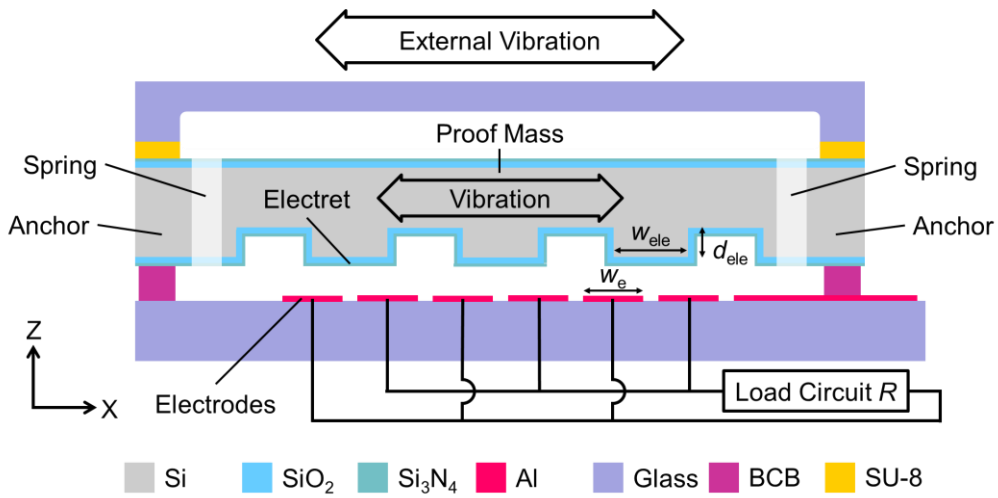


**Figure 5.1.** Schematic cross-sectional view of electrostatic MEMS vibration energy harvester.

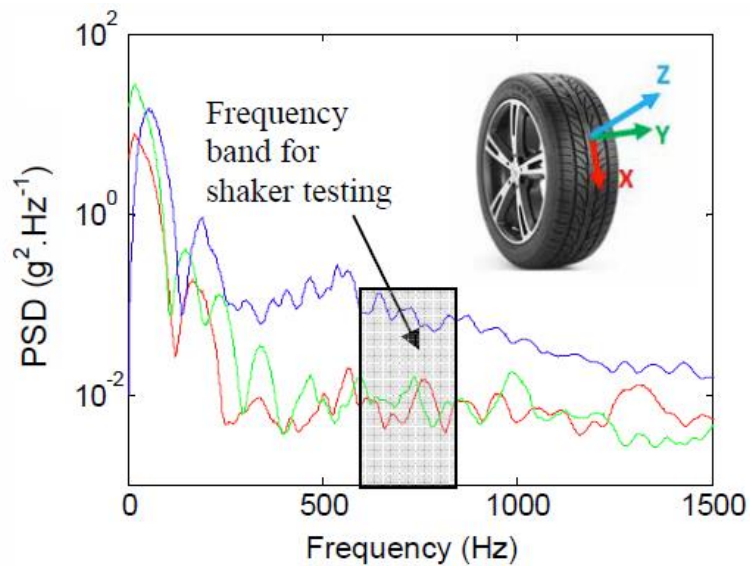


**Figure 5.2.** PSD (power spectral density) of impact vibration acceleration inside of the tire tread in the case of a traveling speed of 60 km/h.

### 5.2.2. Electrode Configuration for High Power Generation

The convex portion of the electret is arranged to face the two output electrodes with the same overlap area. When the proof mass is displaced by the external vibration, the overlap area of the two opposed portions changes, keeping the total opposed area the same. For example, when the area of one facing part increases with a certain value, the area of the other facing part decreases with the same value. The maximum displacement of the proof mass is  $100\ \mu\text{m}$  according to the expansion and contraction of the Si spring. A width of the convex portion of the electret is  $w_{\text{ele}} = 250\ \mu\text{m}$ . In this case, the output electrode width is designed to be  $w_e = 200\ \mu\text{m}$  so that the convex portion displaces within the two opposed output electrodes. Even when the displacement reaches the maximum value, the configuration is designed so as not to displace up to the third output electrode. An electrostatic capacitance between the electret and the one side output electrode changes linearly with respect to the relative displacement. An output signal waveform can be made into a regular sinusoidal wave in order to reduce power loss with the electromechanical linearity [18,19]. A glass insulator is used as the lower substrate for the reduction of parasitic capacitance between the output electrodes and the substrate, which is also effective to increase the power generation, avoiding signal transmission loss.

### 5.2.3. Electret Structure for a High Charge Ratio on Output Electrodes

The corrugated electret structure is one of features of this developed generator. Conventionally, the electret material is patterned on a flat surface

in order to ensure an electric potential difference on the output electrode between the state in which the electret and the output electrode are opposed and the state in which they are not opposed to each other [20]. The electric field of the patterned electret is quite homogeneous due to a fringing field, and it is the cause of the degradation of the electric potential difference between narrow rectangular electrets and spaces. The electret material is deposited on the corrugated structure without the necessity of the electret patterning.

A capacitance change can be obtained since the distance from the convex portion or the concave portion to the output electrode varies. The simulated capacitance change as a function of depth of the corrugated electret is shown in Figure 5.3. A depth of the concave portion of the electret is optimized to  $d_{ele} = 100 \mu\text{m}$  to saturate the capacitance change. It is possible to change the amount of induced charges on the output electrodes and to obtain high power generation capability with this configuration. The designed specifications are summarized in Table 5.1.

It is supposed as a note that the non-uniform fringing electric fields of the corrugated electret also have an influence on the movement of the proof mass, even for a submicron irregular displacement, which is linked to energy damping [21].

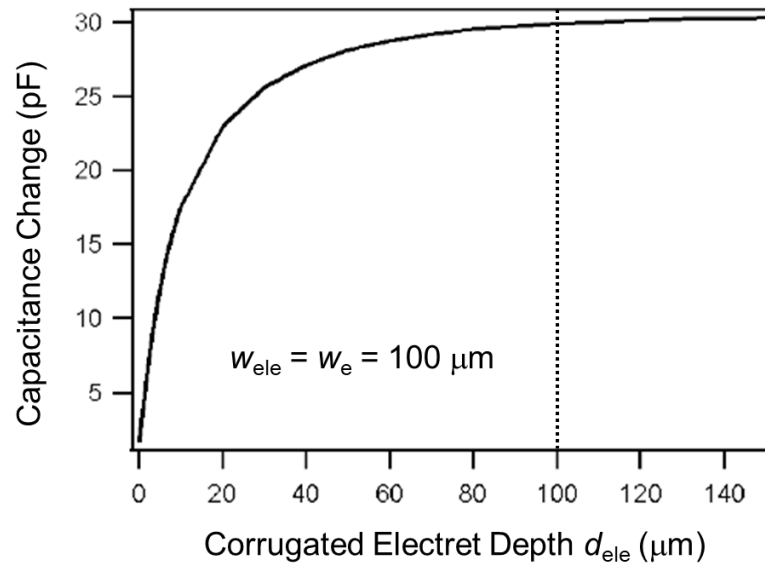


**Figure 5.3.** Simulated capacitance change as a function of depth of corrugated electret.

**Table 5.1.** Designed specifications of electret transducers in MEMS vibration energy harvesters.

<b>Electret Transducer</b>	
Corrugated Electret Width ( $w_{ele}$ )	250 $\mu\text{m}$
Corrugated Electret Depth ( $d_{ele}$ )	100 $\mu\text{m}$
Electrode Width ( $w_e$ )	200 $\mu\text{m}$
Electrode Space	50 $\mu\text{m}$
Gap	10 $\mu\text{m}$
Electret Maximum Displacement	100 $\mu\text{m}$

## 5.3. Fabrication

### 5.3.1. Process Flow

The fabrication process flow for the energy harvesters is shown in Figure 5.4. Firstly, the surface of the middle Si substrate was deeply etched  $d_{\text{ele}} = 100 \mu\text{m}$  by DRIE (deep reactive ion etching) to form a corrugated structure. Then, 1  $\mu\text{m}$ -thick  $\text{SiO}_2$  and 150 nm-thick  $\text{Si}_3\text{N}_4$  as the electret materials were grown covering the corrugated structure. The proof mass and the springs were formed by DRIE through the whole thickness of 650  $\mu\text{m}$  of the substrate. The  $\text{SiO}_2/\text{Si}_3\text{N}_4$  stacked film was used as the hard mask for the DRIE. The Si spring has a high aspect ratio in the thickness direction. The electret side of the substrate was discharged by a corona discharger to functionalize as an electret. A close-up SEM image of the spring area is shown in Figure 5.5a. An optical microscope image of the proof mass and the spring during vibration is shown in Figure 5.5b.

An Al electrode was formed on a glass substrate as the lower substrate, which was bonded to the middle substrate via BCB (benzocyclobutene). The distance between the electret and the output electrode was adjusted to 10  $\mu\text{m}$  with a thickness of the BCB bonding frame patterned using photolithography. The bonding resin (SU-8) was formed by roller coating on the top glass substrate that was partially engraved, and the top substrate was bonded to and packaged with the middle substrate via the SU-8.

### 5.3.2. Annealing Process for a Highly-Stable Inorganic Electret

In order to improve the charge retention stability of the electret, heat treatment (annealing) was performed after deposition of  $\text{SiO}_2/\text{Si}_3\text{N}_4$  materials. The charge retention stability was evaluated introducing TSC (thermally-stimulated current) measurement. The TSC temperature dependence of the inorganic electret is shown in Figure 5.6. The TSC sharper peak with respect to temperature means higher charge retention stability because higher activation energy was necessary to move the trapped charge. The peak became steep by applying the annealing, the peak width in temperature at TSC  $-2.0$  pA was  $\Delta 50$  K from 620-670 K with annealing and  $\Delta 70$  K from 620-690 K without annealing. It was confirmed that the deep potential wells around 650 K for the stable charge trapping were more uniformly formed.

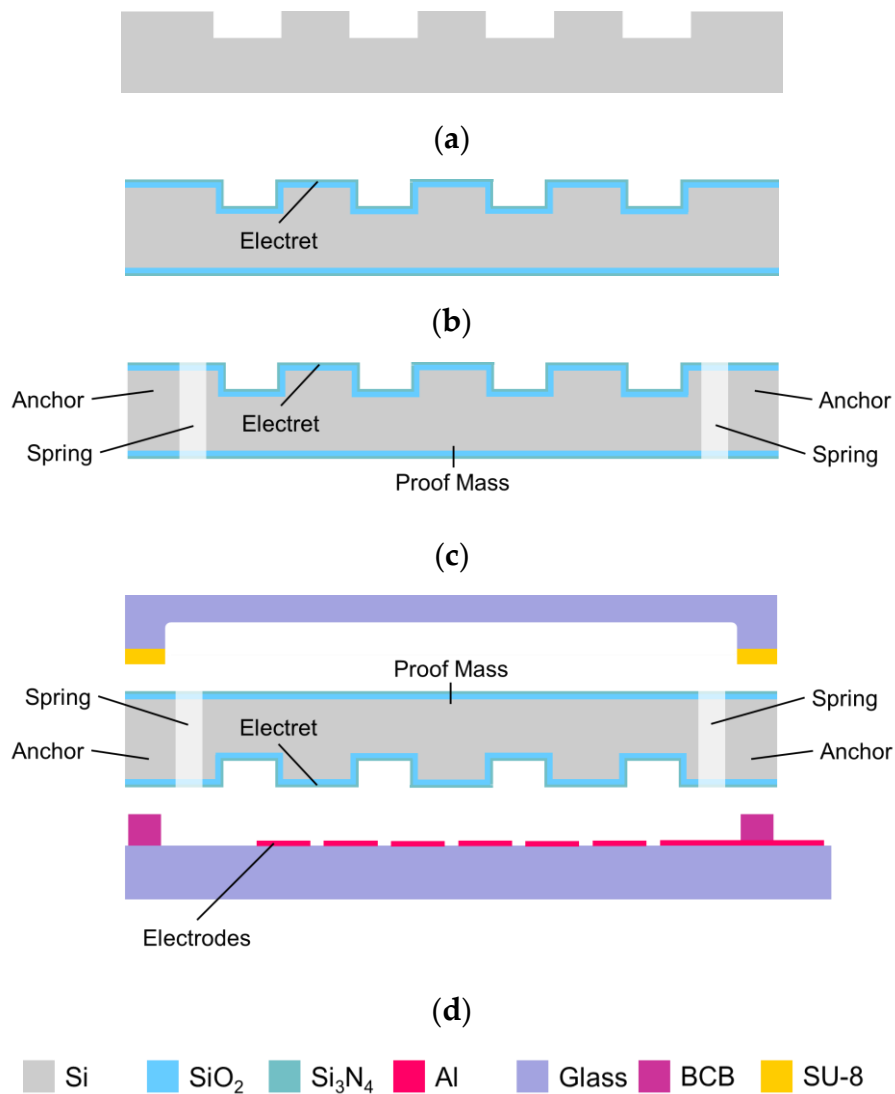
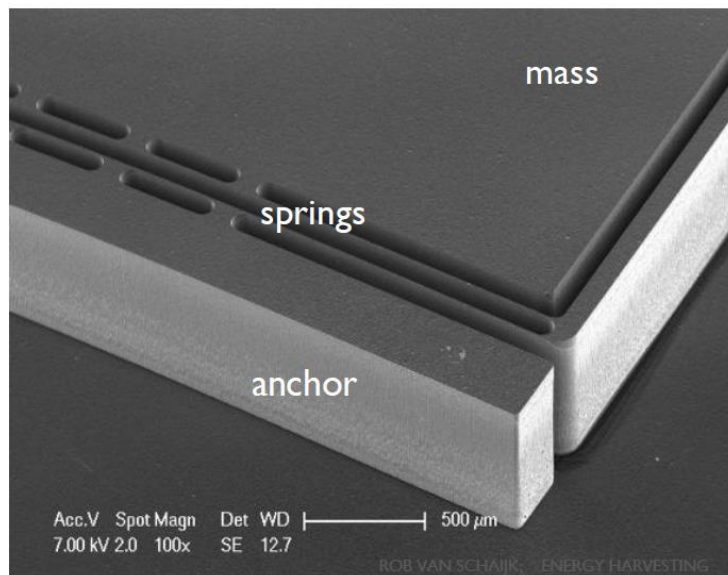
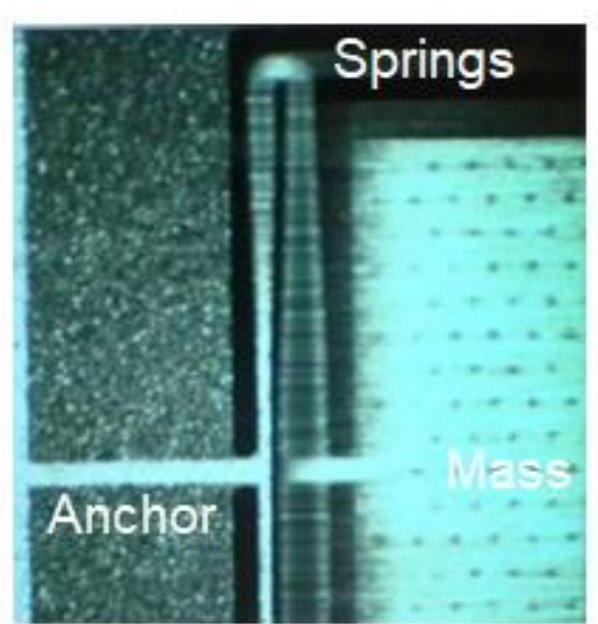


**Figure 5.4.** Fabrication process flow for electrostatic MEMS vibration energy harvester: (a) etching of trenches in Si substrate; (b)  $\text{SiO}_2/\text{Si}_3\text{N}_4$  thermal growth as electret; (c) etching through Si substrate to define springs, and corona discharging to electret; (d) formation of Al electrodes and BCB bonding frame on the bottom glass substrate, formation of SU-8 bonding frame on the partially engraved top glass substrate, and bonding Si substrate with glass substrates.



(a)



(b)

**Figure 5.5.** Fabricated electrostatic MEMS vibration energy harvester: (a) close-up SEM images of spring area; (b) optical microscope image of the proof mass and spring during vibration.

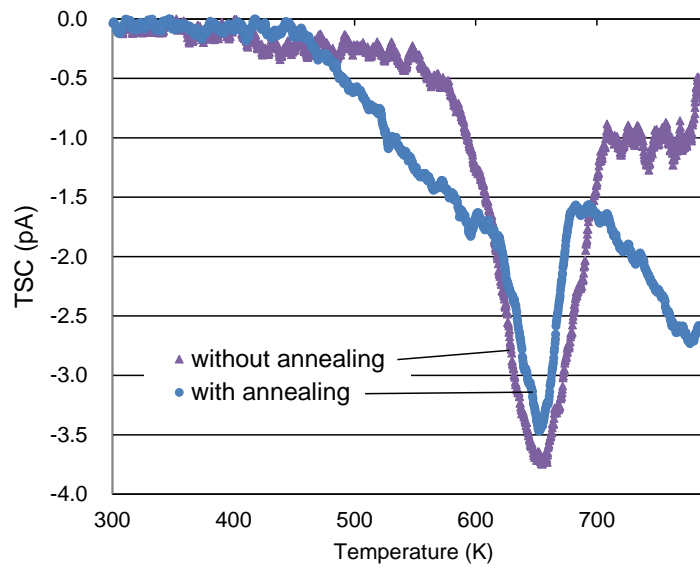


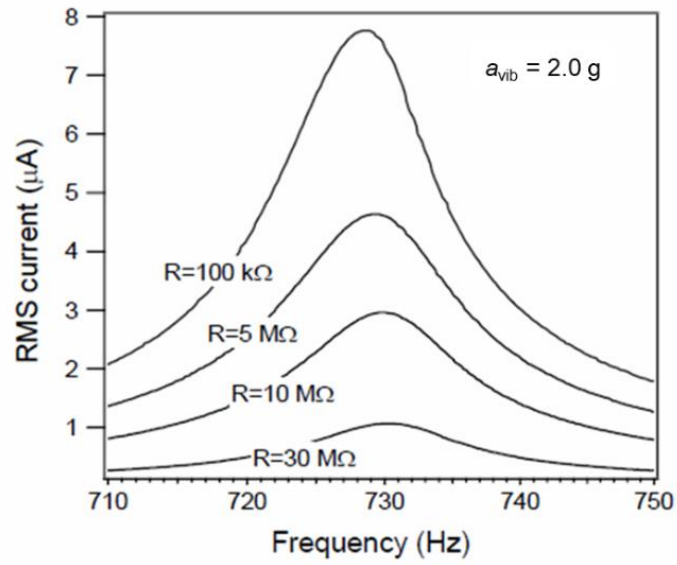
**Figure 5.6.** TSC (thermally-stimulated current) spectrum of the electret SiO<sub>2</sub>/Si<sub>3</sub>N<sub>4</sub> stacked film.

## 5.4. Measurement Result

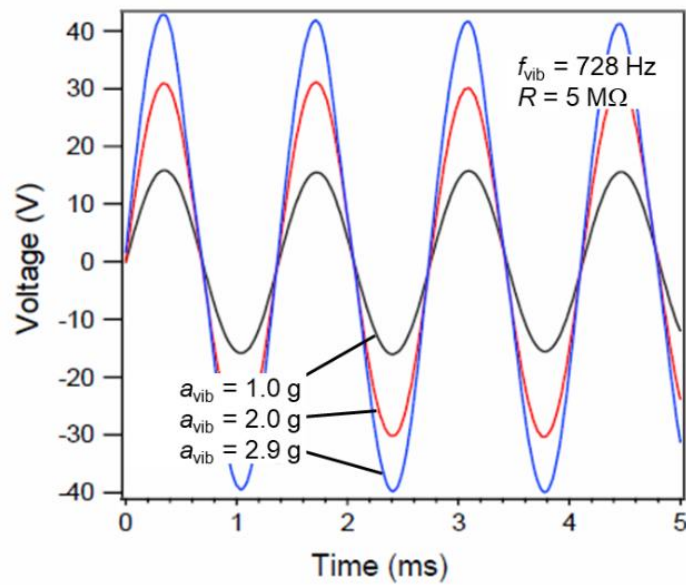
### 5.4.1. Sign-Wave Vibration

The basic performance of the fabricated energy harvesters was evaluated under sinusoidal vibration. The frequency response and output voltage waveform are shown in Figure 5.7a,b. The RMS (root mean square) value of the output current  $i_{rms}$  had a Lorentzian shape and good linearity with respect to the frequency of external vibration. The proof mass, the mechanical resonant frequency of the first mode, and the electret potential were  $m = 160$  mg,  $f_{vib} = 728$  Hz, and  $V_{ele} = 120$  V, respectively. The frequency of the external vibration was adjusted to the mechanical resonant frequency, and the acceleration of the external vibration was changed. For the output current  $i_{rms}$  flowing through load resistance  $R$ , the average output power  $P$  can be calculated with the relation of  $P = R \times i_{rms}^2$ . The load matching was achieved at the load resistance  $R = 5$  M $\Omega$ . The output voltage amplitude varied linearly with the vibration acceleration. The output voltage amplitude reached the maximum value of 41 V when the proof mass reached the maximum displacement with the vibration acceleration  $a_{vib} = 2.9$  g.

On the fabricated energy harvesters, the parameters were increased to the ideal mechanical resonance frequency  $f_{vib} = 1.2$  kHz and  $V_{ele} = 200$  V. The vibration acceleration dependence of the output power is shown in Figure 5.8. The high output power of  $P = 495$   $\mu$ W was obtained although the footprint size was as small as about  $A_{dev} = 1$  cm<sup>2</sup>.



(a)



(b)

**Figure 5.7.** Evaluation of the fabricated electrostatic MEMS vibration energy harvester: (a) frequency response; (b) output voltage of vibration frequency of 728 Hz, electret potential of 120 V, and road resistance of  $5 \text{ M}\Omega$ .

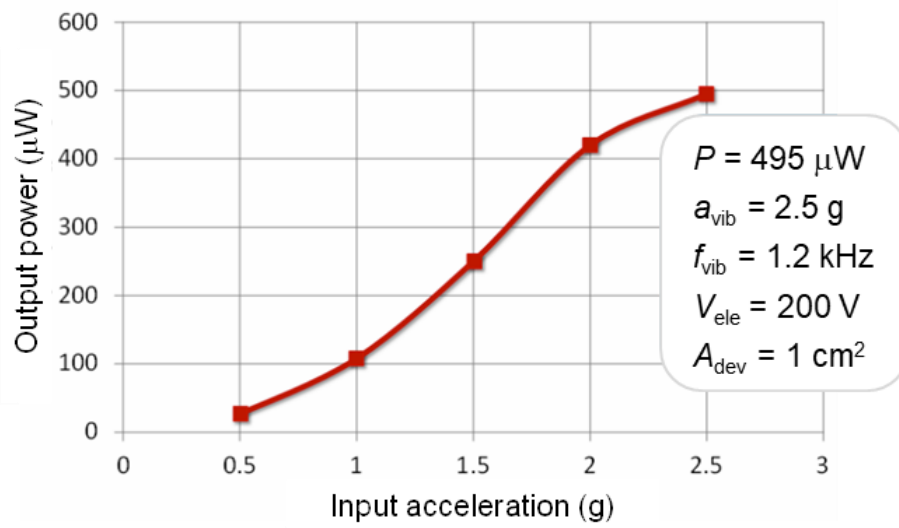


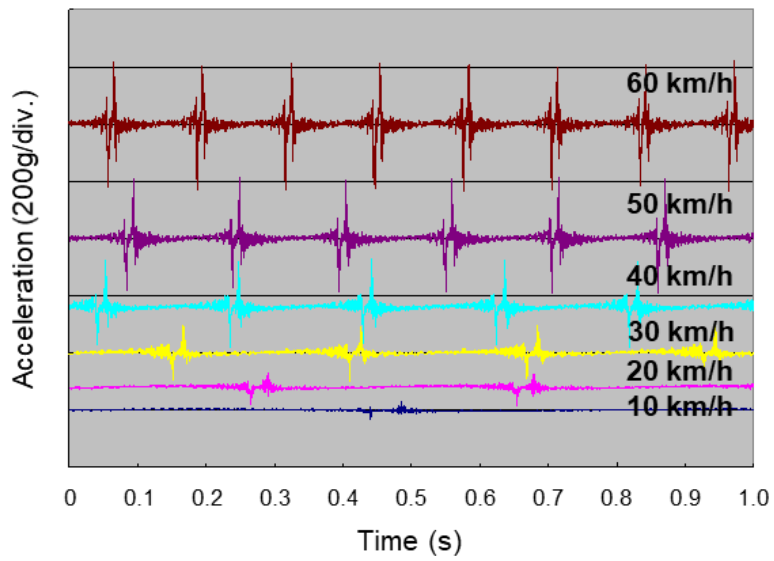
**Figure 5.8.** Output power of the fabricated electrostatic MEMS vibration energy harvester of a vibration frequency of 1.2 kHz and an electret potential of 200 V.

#### 5.4.2. Impact Vibration in Tire Tread

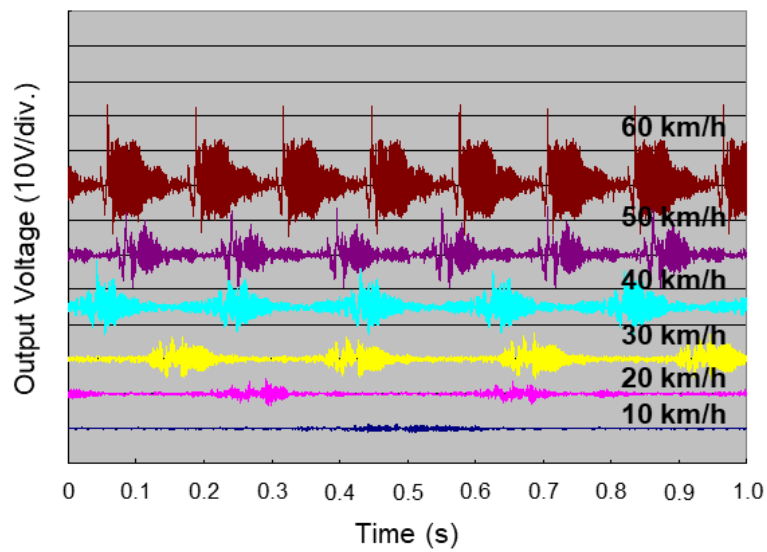
In order to detect information from the road surface more accurately, a tire sensor was mounted inside of the tire tread. The performances of the fabricated energy harvesters had to be evaluated under impact vibration generated when the tire sensor contacted the road surface. In situ measurements were performed by mounting the energy harvester and an accelerometer inside of the tire tread using an adhesive agent. The acceleration sensor measured the vibration in the tangential direction X, the lateral direction Y, and the radial direction Z of the circular tire. It was attempted to harvest the vibration energy in the tire rotation direction X by aligning the vibration direction of the proof mass of the energy harvester.

The measured acceleration of the impact vibration is shown in Figure 5.9a. The impact vibration occurred every time the tire rotated, and the acceleration increased at faster traveling speeds. The output voltage of the energy harvester with the impact vibration is shown in Figure 5.9b. The voltage value became the maximum when the harvester contacted the road surface and then decreased due to free damped oscillation of the proof mass while the harvester detached from the road surface. It was confirmed that the output voltage increased at higher traveling speed. The PSD dependence of the output power is shown in Figure 5.10. The PSD of the impact vibration acceleration was reproduced by an electrodynamic shaker. The output power  $60 \mu\text{W}$  was obtained in spite of the low PSD value of  $5.0 \times 10^{-3} \text{ g}^2 \cdot \text{Hz}^{-1}$  reproduced for a traveling speed of 60 km/h. It was revealed that a higher resonance frequency of spring adjusted to the frequency band of low PSD was effective for high efficiency harvest impact vibration energy.

In the case of the output electrode width  $w_e = 100 \mu\text{m}$ , a capacitance between the electret and the one side output electrode changed non-linearly with respect to relative displacement because the convex portion of the electret reached the next nearest neighbor output electrode when the proof mass reached the maximum displacement. The output wave became an irregular waveform rather than a sinusoidal waveform, and the output power degraded as described in Section 5.2.2. It was confirmed that the electromechanical linearity was effective to increase the power generation.



(a)



(b)

**Figure 5.9.** Evaluation of the electrostatic MEMS vibration energy harvester inside of the tire tread: (a) impact vibration acceleration; (b) output voltage.

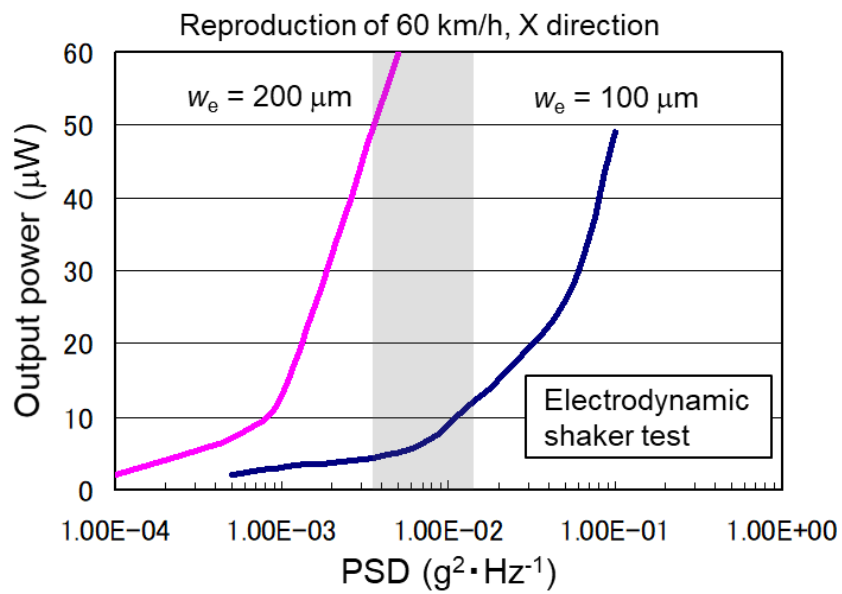


**Figure 5.10.** Output power of the electrostatic MEMS vibration energy harvester depending on the PSD (power spectral density) of impact vibration acceleration inside of the tire tread.

## 5.5. Discussion

In this chapter, the vibration energy harvesters inside of tire treads were described. An inorganic insulator  $\text{SiO}_2/\text{Si}_3\text{N}_4$  film usable in a Si-based CMOS/MEMS production line was used as an electret material. By making the electret into a corrugated structure, a capacitance change could be obtained since the distance from the convex portion or the concave portion to the output electrode varied. It was possible to change the amount of induced charges on the output electrodes. In addition, the device was designed to change the capacitance between the convex portion of the electret and the output electrode linearly with displacement of the proof mass. The electromechanical linearity was effective at reducing the power loss. The output power reached  $495 \mu\text{W}$  under sinusoidal vibration at an adjusted high frequency  $1.2 \text{ kHz}$  despite the footprint size being as small as  $1 \text{ cm}^2$ .

Under impact vibration inside of the tire tread, the output power reached  $60 \mu\text{W}$  in the case of PSD  $5.0 \times 10^{-3} \text{ g}^2 \cdot \text{Hz}^{-1}$  at a traveling speed of  $60 \text{ km/h}$ . The performance was an order of magnitude higher output power in spite of an order of magnitude lower PSD compared to previous works. It was revealed that the higher mechanical resonance frequency of the harvester adjusted within the frequency band of low PSD was effective for high efficiency harvest impact vibration energy inside of the tire tread. A reliability test will be done to confirm whether the MEMS vibration energy harvesters are durable against a shock inside of the tire treads.

One of the issues for practical use is a power management circuit. The AC (alternating current) generated from the vibration energy harvester

has to be converted to DC using an AC/DC converter in order to use the energy harvester as a DC power supply. A high efficiency AC/DC converter was developed to deal with the high output voltage of the electrostatic generator. The MPPT (maximum power point tracking) technology was introduced to realize a high conversion efficiency of 88 % [22]. In addition, this is a concept of self-starting by generated power, which can eliminate an activating circuit. The vibration energy harvester could be used as a DC power supply for tire sensors.

In further work, it is expected that electrostatic MEMS vibration energy harvesters inside of tire treads will enhance the function of tire sensors, which will enable the evolution of intelligent automobiles.

## References

1. Löhndorf, M.; Kvisterøy, M T.; Westby, E.; Halvorsen, E. Evaluation of energy harvesting concepts for tire pressure monitoring systems. In Proceedings of the PowerMEMS 2007, Freiburg, Germany, 28-29 November 2007; pp. 331-334.
2. Westby, E.R.; Halvorsen, E. Design and modeling of a patterned-electret-based energy harvester for tire pressure monitoring systems. *IEEE/ASME Trans. Mechatron.* 2012, 17, 995-1005.
3. Jones, T.B. Lumped parameter electromechanics of electret transducers. *IEEE Trans. Acoust. Speech Signal Process.* 1974, 22, 141-145.
4. Suzuki, Y. Recent progress in MEMS electret generator for energy harvesting. *IEEJ Trans. Electr. Electron. Eng.* 2011, 6, 101-111.
5. Boisseau, S.; Despesse, G.; Seddik, B.A. Electrostatic conversion for vibration energy harvesting. In *Small-Scale Energy Harvesting*; Lallart, M., Ed.; IntechOpen: London, UK, 2012; pp. 91-134, ISBN 978-953-51-0826-9.
6. Sakane, Y.; Suzuki, Y.; Kasagi, N. The development of a high-performance perfluorinated polymer electret and its application to micro power generation. *J. Micromech. Microeng.* 2008, 18, 104011.
7. Renaud, M.; Altena, G.; Goedbloed, M.; de Nooijer, C.; Matova, S.; Naito, Y.; Yamakawa, T.; Takeuchi, H.; Onishi, K.; van Schaijk, R. A high performance electrostatic MEMS vibration energy harvester with corrugated inorganic SiO<sub>2</sub>-Si<sub>3</sub>N<sub>4</sub> electret. In Proceedings of the 17th International Conference on Solid-State Sensors, Actuators and

- Microsystems (TRANSDUCERS & EUROSENSORS XXVII), Barcelona, Spain, 16-20 June 2013; pp. 693-696.
8. Takahashi, T.; Suzuki, M.; Hirata, T.; Matsushita, N.; Yoneya, R.; Onishi, J.; Nishida, T.; Yoshikawa, Y.; Aoyagi, S. Electret energy harvesting based on fringe electrical field change inside trenched ferroelectric. In Proceedings of the 2011 IEEE 24th International Conference on Micro Electro Mechanical Systems, Cancun, Mexico, 23-27 January 2011; pp. 1305-1308.
  9. Kittipaisalsilpa, K.; Kato, T.; Suzuki, Y. Liquid-crystal-enhanced electrostatic vibration generator. In Proceedings of the 2016 IEEE 29th International Conference on Micro Electro Mechanical Systems (MEMS), Shanghai, China, 24-28 January 2016; pp. 37-40.
  10. Tao, K.; Wu, J.; Tang, L.; Hu, L.; Lye, S.W.; Miao, J. Enhanced electrostatic vibrational energy harvesting using integrated opposite-charged electrets. *J. Micromech. Microeng.* 2017, 27, 044002.
  11. Koga, H.; Mitsuya, H.; Toyama, Y., Sugiyama, T.; Toshiyoshi, H.; Hashiguchi, G. Development of a metal-cantilever electrostatic vibration power generator combined with potassium ion electret technique. In Proceedings of the 2018 Joint International Conference on Information Storage and Processing Systems and Micromechatronics for Information and Precision Equipment, San Francisco, CA, USA, 29-30 August 2018; pp. 1-3.
  12. Asanuma, H.; Hara, M.; Oguchi, H.; Kuwano, H. Air gap optimization for output power and band width in out-of-plane vibration energy harvesters employing electrets. *J. Micromech. Microeng.* 2015, 25, 104013.

13. Tao, K.; Lye, S.W.; Miao, J.; Tang, L.; Hu, X. Out-of-plane electret-based MEMS energy harvester with the combined nonlinear effect from electrostatic force and a mechanical elastic stopper. *J. Micromech. Microeng.* 2015, 25, 104014.
14. Asanuma, H.; Hara, M.; Oguchi, H.; Kuwano, H. Nonlinear restoring force of spring with stopper for ferroelectric dipole electret-based electrostatic vibration energy harvesters. *AIP Adv.* 2016, 6, 075206.
15. Basset, P.; Galayko, D.; Cottone, F.; Guillemet, R.; Blokhina, E.; Marty, F.; Bourouina, T. Electrostatic vibration energy harvester with combined effect of electrical nonlinearities and mechanical impact. *J. Micromech. Microeng.* 2014, 24, 035001.
16. Zhang, Y.; Luo, A.; Xu, Y.; Wang, T.; Zhang, A.; Wang, F. Electret-based electrostatic energy harvesting device with the MEMS technology. In *Proceedings of the 2016 12th IEEE/ASME International Conference on Mechatronic and Embedded Systems and Applications (MESA)*, Auckland, New Zealand, 29-31 August 2016; pp. 1-6.
17. Sterken, T.; Fiorini, P.; Baert, K.; Puers, R.; Borghs, G. An electret-based electrostatic  $\mu$ -generator. In *Proceedings of the 12th International Conference on Solid-State Sensors, Actuators and Microsystems*, Boston, MA, USA, 8-12 June 2003; pp. 1291-1294.
18. Jefimenko, O. Slot effect in electret devices. *Proc. W. Va. Acad. Sci.* 1968, 40, 345-348.
19. Gerhard-Multhaupt, R. Theoretical and experimental study of the electromechanical electret slit-effect transducer. *J. Phys. D Appl. Phys.* 1984, 17, 649-663.

20. Genda, T.; Tanaka, S.; Esashi M. High power electret motor and generator on shrouded turbine. In Proceedings of the PowerMEMS 2004, Kyoto, Japan, 28-30 November 2004; pp. 183-186.
21. Mitcheson, P.D.; Green, T.C.; Yeatman, E.M.; Holmes, A.S. Architectures for vibration-driven micropower generators. *J. Microelectromech. Syst.* 2004, 13, 429-440.
22. Stanzione, S.; van Liempd, C.; van Schaijk, R.; Naito, Y.; Yazicioglu, F.; Van Hoof, C. A high voltage self-biased integrated DC-DC buck converter with fully analog MPPT algorithm for electrostatic energy harvesters. *IEEE J. Solid-State Circuits* 2013, 48, 3002-3010.

## Chapter 6. Conclusion

This thesis revealed that novel bi-directional transducers could realize low voltage RF-MEMS switches, low voltage MEMS resonators and high output MEMS energy harvesters for wireless sensors.

In Chapter 2, the capacitive RF-MEMS switching devices utilizing comb-drive electrodes for low voltage actuation and fast response were described. The process flow for MEMS fabrication was optimized considering compatibility in the 0.18  $\mu\text{m}$  CMOS BEOL process on a 200 mm substrate toward low-cost fabrication and integrated MEMS devices with CMOS circuits. The switching devices were fabricated using a simple low-cost two-mask process. The comb-drive electrodes and the lower electrodes allow the suspended membrane to move vertically upward as well as downward entirely by the electrostatic forces, thus enabling a fast overall response in MEMS devices. The measured C-V and RF characteristics were  $C_{\text{down}} / C_{\text{up}} = 0.514 \text{ pF} / 0.095 \text{ pF} = 5.4$ , and the transmission parameter  $S_{21}$  in the down-state and the up-state is  $-2.4 \text{ dB}$  and  $-15.1 \text{ dB}$  at 5 GHz, respectively. The measured responses were 4.5  $\mu\text{s}$  into the down-state and 8.0  $\mu\text{s}$  into the up-state with 5 V actuation voltage. The continuous drive cycles characteristics were measured up to  $10^9$  cycles, in which stable actuation was observed up to  $10^7$ ; degradation of actuation into the up-state was observed from an order of  $10^8$  cycles. It was revealed that the MEMS devices using the effective comb-drive actuation for low voltage actuation and fast response are embodied with the CMOS process, which could contribute to low-cost integrated RF-MEMS switches, switched capacitors and MEMS devices in circuits for expected applications.

In Chapter 3, the laterally movable triple electrodes actuator in capacitive series shunt hybrid RF-MEMS switches for a low voltage actuation and fast response were described. The actuator allows all of the suspended beams to move laterally in two directions entirely by electrostatic forces. The switches were fabricated using a simple, low-cost two-mask process with sputtered aluminum as the structural material. The measured response time and the actuation voltage were 5.0  $\mu\text{s}$  and 9 V, respectively. Consequently, it was revealed that the laterally movable triple electrodes actuator is effective toward the lower actuation voltage than 10 V and the faster response than 10  $\mu\text{s}$  in RF-MEMS switches. It is expected that the actuator advances RF-MEMS switches, switched capacitors, and MEMS devices in circuits for wireless sensor networks.

In Chapter 4, the torsional-mode single crystalline silicon triangular beam resonators, vacuum encapsulated using a thin SiGe film were described. The resonator was demonstrated displaying a stable high- $Q$  (of around 220,000) with a low driving voltage (1 V) and low motional resistance ( $< 12 \text{ k}\Omega$ ). The triangular shaped beam was realized by an anisotropic etch of Si on SOI wafer. A 4  $\mu\text{m}$  thick SiGe thin film was used for the base capping layer such that the thin film package offers sufficient strength against transfer molding pressures of at least 10 MPa. Sputter deposited Al is used to seal the cavity at a pressure of 1 Pa. The  $Q$  value did not show noticeable change for over 4,000 hours. A fabricated CMOS-based oscillator using the MEMS torsional resonator was also demonstrated as the frequency determining element. Such high- $Q$  MEMS resonators with low motional resistance and low driving voltage turn out to be advantageous to attain high frequency accuracy of a reference oscillator with a low power consumption.

In Chapter 5, the vibration energy harvesters inside of tire treads were described. An inorganic insulator  $\text{SiO}_2/\text{Si}_3\text{N}_4$  film usable in a Si-based CMOS/MEMS production line was used as an electret material. The device was designed to change the capacitance between the convex portion of the electret and the output electrode linearly with displacement of the proof mass. The electromechanical linearity was effective at reducing the power loss. The output power reached  $495 \mu\text{W}$  under sinusoidal vibration at an adjusted high frequency  $1.2 \text{ kHz}$  despite the footprint size being as small as  $1 \text{ cm}^2$ . Under impact vibration inside of the tire tread, the output power reached  $60 \mu\text{W}$  in the case of PSD  $5.0 \times 10^{-3} \text{ g}^2 \cdot \text{Hz}^{-1}$  at a traveling speed of  $60 \text{ km/h}$ . The performance was an order of magnitude higher output power in spite of an order of magnitude lower PSD compared to previous works. It was revealed that the higher mechanical resonance frequency of the harvester adjusted within the frequency band of low PSD was effective for high efficiency harvest impact vibration energy inside of the tire tread. In further work, it is expected that electrostatic MEMS vibration energy harvesters will enhance the function of tire sensors, which will enable the evolution of intelligent automobiles.

This thesis revealed solutions that realize low voltage RF-MEMS switches, low voltage MEMS resonators and high output MEMS energy harvesters for autonomous wireless sensor module, which could reduce power consumption of electronic circuits and increase power of the generator in order to compensate the whole power consumed in the module. It is expected to provide highly convenient functions and services by the autonomous wireless sensor modules implemented to IoT, M2M and Trillion Sensors Universe in the future.



## Acknowledgement

In promoting this doctoral thesis, the author would like to acknowledge supervisor and chief examiner Prof. Dr. Keisuke Uenishi. And also, the author would like to acknowledge sub-chief examiners Prof. Dr. Takao Yamamoto, Asso. Prof. Dr. Hiroaki Mori at Department of Management of Industry and Technology, Graduate School of Engineering, Osaka University, and Asso. Prof. Dr. Shinji Fukumoto at Division of Materials and Manufacturing Science, Graduate School of Engineering, Osaka University.

Moreover, it was difficult to achieve this study without cooperation of joint researchers Prof. Dr. Hideki Kawakatsu at Institute of Industrial Science, University of Tokyo, Principal Researcher Dr. Harrie A. C. Tilmans at imec, Principal Researcher Dr. Rob van Schaijk at imec Netherland (previous affiliation), and other members of their teams. I would like to acknowledge all of them for valuable contribution.

This study was conducted by management decision of resources and technical supports of Technology Innovation Division, Panasonic Corporation to which the author belongs. The author would like to thank Director Dr. Eiji Fujii, General Manager Dr. Masa-aki Suzuki, Strategic Planning Manager Mr. Keiji Onishi, Staff Researcher Mr. Kunihiko Nakamura, and other colleagues of research projects for giving this opportunity.

Finally, I would like to thank my parents, my wife, my son, my daughter and my family who understand my degree and cooperate in my life.

## **Publications Related to This Thesis**

### **Journals**

1. Naito, Y.; Nakamura, K.; Onishi, K. RF-MEMS switching devices using vertical comb-drive actuation in the CMOS process. *J. Micromech. Microeng.* 2010, 20, 045001.
2. Nakamura, K.; Naito, Y.; Onishi, K.; Kawakatsu, H. A high-quality factor of 267 000 micromechanical silicon resonator utilizing TED-free torsional vibration mode. *J. Micromech. Microeng.* 2012, 22, 125028.
3. Naito, Y.; Nakamura, K.; Uenishi, K. Laterally movable triple electrodes actuator toward low voltage and fast response RF-MEMS switches. *Sensors* 2019, 19, 4, 864.
4. Naito, Y.; Uenishi, K. Electrostatic MEMS vibration energy harvesters inside of tire treads. *Sensors* 2019, 19, 4, 890.

### **International Conferences**

1. Naito, Y.; Shimizu, N.; Hashimura, A.; Nakamura, K.; Nakanishi, Y. A low-cost vertical comb-drive approach to low voltage and fast response RF-MEMS switches. In *Proc. the 34th European Microwave Conference (EuMC)*, Amsterdam, The Netherlands, 12-14 October 2004; vol. 3, pp. 1149-1152.
2. Naito, Y.; Helin, P.; Nakamura, K.; De Coster, J.; Guo, B.; Haspeslagh, L.; Onishi, K.; Tilmans, H.A.C. High-Q torsional mode Si triangular beam resonators encapsulated using SiGe thin film. In *Tech. Dig. IEEE Int.*

Electron Device Meeting (IEDM), San Francisco, CA, USA, 5-7 December  
2010; pp. 154-157.

## Other Publications

### Journals

1. Itoh, H.; Naito, Y.; Inoue, J. Numerical study of magnetoresistance in ferromagnetic tunnel junctions with disordered barrier. *J. Magnetics Society of Japan* 2000, 24, 587-590 (in Japanese).
2. Naito, Y.; Itoh, H.; Inoue, J. Conductance in magnetic nano-wires. *Surface Science* 2001, 493, 591-596.
3. Stanzione, S.; van Liempd, C.; van Schaijk, R.; Naito, Y.; Yazicioglu, F.; Van Hoof, C. A high voltage self-biased integrated DC-DC buck converter with fully analog MPPT algorithm for electrostatic energy harvesters. *IEEE J. Solid-State Circuits* 2013, 48, 12, 3002-3010.
4. Naito, Y.; Onishi, K. Vibration energy harvesters with inorganic electret. *Function & Materials* 2015, 35, 3, 39-44 (in Japanese).

### International Conferences

1. Naito, Y.; Itoh, H.; Inoue, J. Conductance in magnetic nano-wires. *Int. Symp. on Surface and Interface – Properties Different Symmetry Crossing (ISSI PDSC)*, Nagoya, Japan, 17-20 October 2000.
2. Itoh, H.; Naito, Y.; Inoue, J. Spin-dependent transport in ferromagnetic nanowires. *Int. Symp. on Metallic Multilayers (MML)*, Aachen, Germany, 24-29 June 2001.
3. Naito, Y.; Helin, P.; Nakamura, K.; De Coster, J.; Haspeslagh, L.; Onishi, K.; Tilmans, H.A.C. High-Q micromechanical resonators using thin film

- encapsulation. The 7th Int. Nanotechnology Conference on Communication and Cooperation (INC7), Albany, NY, USA, 16-19 May 2011.
4. Helin, P.; Verbist, A.; De Coster, J.; Guo, B.; Severi, S.; Witvrouw, A.; Haspeslagh, L.; Tilmans, H.A.C.; Naito, Y.; Nakamura, K.; Onishi, K. A wafer-level poly-SiGe-based thin film packaging technology demonstrated on a SOI-based high-Q MEM resonator. In Proc. Int. Solid-State Sensors, Actuators and Microsystems Conference (TRANSDUCERS), Beijing, China, 5-9 June 2011; pp. 982-985.
  5. Bogaerts, L.; Phommahaxay, A.; Rottenberg, X.; Naito, Y.; De Coster, J.; Varela Pedreira, O.; Van Hoovels, N.; Cherman, V.; Helin, P.; Onishi, K.; Tilmans, H.A.C. A MEMS 0-level packaging technology based on CuSn/Cu chip capping bonding, Micromechanics and Microsystems Europe Workshop (MME), Toensberg, Norway, 19-22 June 2011.
  6. Phommahaxay, A.; Bogaerts, L.; Naito, Y.; Van Cauwenberghe, M.; Tutunjyana, N.; Onishi, K.; Tilmans, H.A.C. Thin MEMS packages obtained by a novel collective cap transfer process. EUROSENSORS, Athens, Greece, 4-7 September 2011.
  7. Renaud, M.; Altena, G.; Goedbloed, M.; de Nooijer, C.; Matova, S.; Naito, Y.; Yamakawa, T.; Takeuchi, H.; Onishi, K.; van Schaijk, R. A high performance electrostatic MEMS vibration energy harvester with corrugated inorganic SiO<sub>2</sub>-Si<sub>3</sub>N<sub>4</sub> electret. In Proc. the 17th Int. Conference on Solid-State Sensors, Actuators and Microsystems (TRANSDUCERS), Barcelona, Spain, 16-20 June 2013; pp. 693-696.
  8. Stanzione, S.; van Liempd, C.; van Schaijk, R.; Naito, Y.; Yazicioglu, R.F.; Van Hoof, C. A self-biased 5-to-60 V input voltage and 25-to-1600 W integrated DC-DC buck converter with fully analog MPPT algorithm

reaching up to 88% end-to-end efficiency. In IEEE Int. Solid-State Circuits Conference (ISSCC) Dig. Tech. Papers, San Francisco, CA, USA, 17-21 February 2013; pp. 74-75.

9. Takahashi, K.; Kawasaki, T.; Tambo, N.; Fujikane, M.; Nakamura, K.; Naito, Y.; Liao, Y.; Kashiwagi, M.; Shiomi, J. Impact of ultrafine nanostructuring on the phonon wave transport of Si phononic crystals. A Meeting of Materials Research Society (MRS), Boston, MA, USA, 25-30 November 2018.
10. Tambo, N.; Zhou, C.; Ashley, E.M.; Liao, Y.; Takahashi, K.; Naito, Y.; Shiomi, J.; Nealey, P.F. Suppression of propagon heat transport in amorphous silicon nitride phononic crystals. A Meeting of Materials Research Society (MRS), Phoenix, AZ, USA, 22-26 April 2019.

### **Domestic Conferences**

1. Itoh, H.; Naito, Y.; Inoue, J. Numerical Study of TMR with disordered barrier. The Physical Society of Japan, Iwate Univ., 24-27 September 1999 (in Japanese).
2. Itoh, H.; Naito, Y.; Inoue, J. Numerical Study of Magnetoresistance in Ferromagnetic Tunnel Junctions with disordered Barrier. The Magnetism Society of Japan, Kitakyushu International Conference Center, 5-8 October 1999 (in Japanese).
3. Naito, Y.; Itoh, H.; Inoue, J. Conductance in ferromagnetic wires: 2-band model. The Physical Society of Japan, Niigata Univ., 22-25 September 2000 (in Japanese).
4. Naito, Y.; Itoh, H.; Inoue, J. Electrical conductance in metallic nano-wires. The Physical Society of Japan, Chuo Univ., 27-30 March 2001 (in

- Japanese).
5. Naito, Y.; Nakamura, K.; Shimizu, N.; Nakanishi, Y. Proposal of RF-MEMS switch structure toward fast response and low voltage actuation. Japanese Society of Applied Physics, Fukuoka Univ., 30 August - 2 September 2003 (in Japanese).
  6. Nakanishi, Y.; Nakamura, K.; Naito, Y.; Shimizu, N.; Hashimura, A. Proposal of RF-MEMS switch structure for mobile terminal. The Institute of Electronics, Information and Communication Engineers, Niigata Univ., 23-26 September 2003 (in Japanese).
  7. Nakamura, K.; Naito, Y.; Shimizu, N.; Nakanishi, Y.; Kawai, S; Kawakatsu, H. Laterally driven RF-MEMS switches consisting of aluminum thin beams. The Japan Society for Precision Engineering, Univ. of Toyama, 2-4 October 2003 (in Japanese).
  8. Naito, Y.; Hashimura, A.; Nakamura, K.; Nakanishi, Y. Fast response and low voltage RF-MEMS switches using simple triple electrodes structure. The Japan Society of Applied Physics, Tohoku Gakuin Univ., 1-4 September 2004 (in Japanese).
  9. Nakanishi, Y.; Naito, Y.; Nakamura, K. Hashimura, A. Proposal of RF-MEMS switches using simple triple electrodes structure. The Institute of Electronics, Information and Communication Engineers, Tokushima Univ., 21-24 September 2004 (in Japanese).
  10. Naito, Y., Hashimura, A.; Nakamura, K.; Nakanishi, Y. Temperature compensation effect of RF-MEMS switches using simple triple electrodes structure. The Japan Society of Applied Physics, Tokushima Univ., 7-11 September 2005 (in Japanese).
  11. Hashimura, A.; Nakamura, K.; Naito, Y.; Nakanishi, Y. Development of torsional-mode RF-MEMS filter. Workshop on Mobile Communication,

The Institute of Electronics, Information and Communication Engineers,  
Yokosuka Research Park, 1-3 March 2006 (in Japanese).

12. Iwasaki, T.; Nakamura, K.; Naito, Y.; Yamakawa, T.; Onishi, K.; Helin, P.; De Coster, J.; Tilmans, H.A.C. Q-factor evaluation methods for atmosphere gas pressure on high-Q MEMS resonators. The Japan Society of Applied Physics, Kanagawa Institute of Technology, 24-27 March 2011 (in Japanese). (Conference canceled)
13. Takeuchi, H.; Nakamura, K.; Naito, Y.; Manaka, T.; Iwamoto, M. A charge distribution in SiO<sub>2</sub>-SiN multilayer evaluated by electric field induced second-harmonic generation. The Japan Society of Applied Physics, Doshisha Univ., 16-20 September 2013 (in Japanese).
14. Naito, Y. Electret vibration energy harvesters for tire sensor. Symposium on Energy Harvesting Technology, TECHNO-FRONTIER, Tokyo Big Sight, 23-25 July 2014 (in Japanese).

## **Books**

1. Naito, Y. (Co-author). Vibration energy harvesters for tire sensors. Recent Design and Application of Energy Harvesting; CMC Publishing Co., Ltd.: Chiyoda City, Tokyo, Japan, 2015; Chapter 15 (in Japanese).







